

Accepted Manuscript

Seasonal variation of Titan's haze at low and high altitudes from HST-STIS spectroscopy

Erich Karkoschka

PII: S0019-1035(15)00298-5

DOI: <http://dx.doi.org/10.1016/j.icarus.2015.07.007>

Reference: YICAR 11639

To appear in: *Icarus*

Received Date: 16 March 2015

Revised Date: 24 June 2015

Accepted Date: 1 July 2015



Please cite this article as: Karkoschka, E., Seasonal variation of Titan's haze at low and high altitudes from HST-STIS spectroscopy, *Icarus* (2015), doi: <http://dx.doi.org/10.1016/j.icarus.2015.07.007>

This is a PDF file of an unedited manuscript that has been accepted for publication. As a service to our customers we are providing this early version of the manuscript. The manuscript will undergo copyediting, typesetting, and review of the resulting proof before it is published in its final form. Please note that during the production process errors may be discovered which could affect the content, and all legal disclaimers that apply to the journal pertain.

Seasonal variation of Titan's haze at low and high altitudes from HST-STIS spectroscopy

Erich Karkoschka

Erich Karkoschka, Lunar and Planetary Laboratory, University of Arizona, Tucson, AZ 85721-0092, USA, phone 1 (520) 621-3994, fax 1 (520) 621-4933, e-mail erich@lpl.arizona.edu

Pages: 61

Figures: 15

Tables: 6

Proposed Running Head: Seasonal variation of Titan's haze using HST-STIS

Highlights:

- > HST-STIS image cubes in five years provide a unique probe of atmospheric variations.
- > The first principal component describes haze opacity variations below 80 km altitude.
- > The second one has similar variations above 150 km but its phase is 1-2 years ahead.
- > The tropics have higher (>150 km) and lower (<80km) opacities than the global mean.
- > The north-south asymmetry may reverse in 2016 (>150 km) and 2017-2018 (<80 km).

Key-words: Titan; Titan atmosphere; Atmospheres, structure; Atmospheres, dynamics; Satellites, atmospheres.

Submitted to Icarus, Special Issue on Titan: 2015-03-15

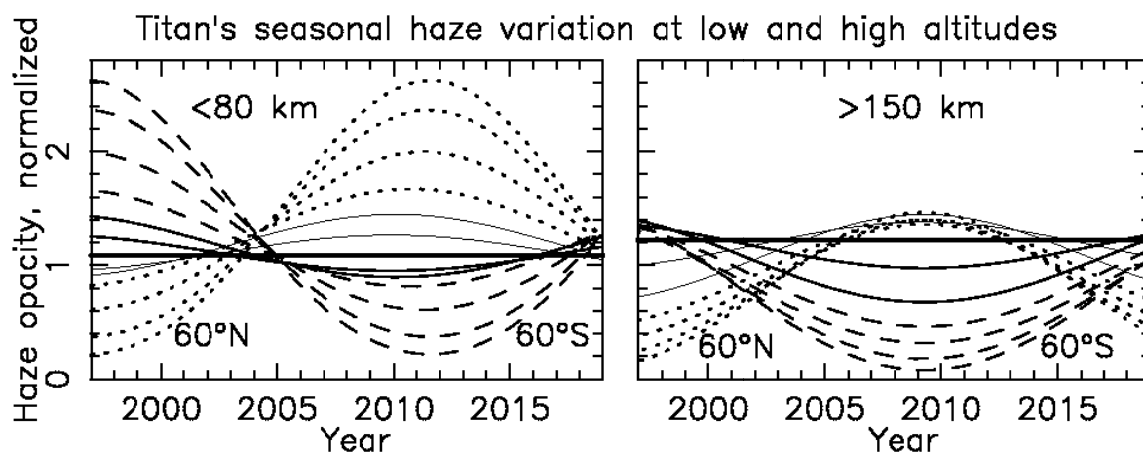
Revised: 2015-06-04, 2015-06-24

Abstract

The Space Telescope Imaging Spectrograph accumulated image cubes of Titan in five years between 1997 and 2004 that we calibrated and analyzed. The observations probe Titan's early northern fall to early winter. Methane bands between 543 and 990 nm wavelength are well resolved spectrally, and Titan's latitudinal and center-to-limb reflectivity variations are resolved spatially. A principal component analysis revealed two large components and two small components of less significance. The first principal component describes a variation of Titan's haze below 80 ± 20 km altitude. Haze particles change their size, opacity, and/or shape of the single scattering phase function. The largest and smallest opacities occurred both in 1997 at high southern latitudes and northern latitudes, respectively. The hemispherical asymmetry switched sign in 2002 at low latitudes, in 2003 at mid latitudes, and in early 2004 at high latitudes. The seasonal amplitude increased almost linearly with distance from the Equator. Tropical latitudes had slightly lower opacities than the annual and global average if the observed variation is seasonally symmetric and shaped like a sine curve. The cause for the variation may be condensation of gases onto aerosols seasonally driven by atmospheric dynamics. The second principal component describes a variation of haze opacity at altitudes above 150 ± 50 km. Largest and smallest opacities both occurred in 2004 at northern and high southern latitudes, respectively. The asymmetry switched in late 2001. Tropical latitudes had significantly higher haze opacity than the annual and global average, opposite to the case at low altitudes. The cause for the high-altitude variation may be aerosols transported at varying speeds driven by atmospheric dynamics. We present a seasonal model that completely describes the haze parameters at each altitude, latitude, and time. It compares fairly well with Cassini results obtained since 2004. The north-south asymmetry may reverse in 2016 at high altitudes and 2017 through 2018 at low altitudes. The observed variations are significant for modeling photometric data of Titan's surface. They

describe several characteristics of Titan's haze variations that can be compared with results from global circulation models.

Graphical Abstract



1. Introduction

Photometry of Titan since 1972 at 472 and 551 nm wavelength indicated a variation that was first correlated with the 11-year solar cycle (Lockwood 1977) but later revealed to be part of an almost periodic variation with a period of 15 years, which is half a Titan year and thus suggests a seasonal variation (Lockwood and Thompson 2009). The phase of the variation excluded the possibility of a pure geometric effect due to changing sub-Earth latitudes.

The Voyager 1 and 2 spacecraft saw Titan obstructed by an almost featureless haze. Most noticeable was that the northern hemisphere was darker than the southern one (Smith *et al.* 1981, 1982). Early Hubble Space Telescope (HST) images in 1990 revealed that the asymmetry had reversed at wavelengths similar to Voyager's filters, but that the asymmetry was opposite in the 889 nm methane filter (Caldwell *et al.* 1992). This wavelength dependence was consistent with models by Toon *et al.* (1992) showing that an increase in haze optical depth causes darkening at wavelengths below 600 nm but brightening at longer wavelengths.

The observed asymmetry explained the phase, but not the amplitude of Titan's photometric variations (Sromovsky *et al.* 1981, 1986, Lockwood *et al.* 1986). Imaging by HST refined the spectral characteristics and caught the next asymmetry reversal (Lorenz *et al.* 1996, 2004).

While there has been work in understanding Titan's seasonal variation through Global Circulation Models (GCM) more recently (Rannou *et al.* 2004, Crespín *et al.* 2008, Lora *et al.* 2015), the best observational constraints on Titan's seasonal variability come from data sets over a sufficiently long time period that spatially resolve Titan's disk. Three data sets are prominent in this respect, data from the Hubble Space Telescope since 1990, from ground-based telescopes with adaptive optics acquiring sufficient spatial resolution about 10 years later (Coustenis *et al.* 2001, Roe *et al.* 2002, Ádámkovics *et al.* 2006), and from the Cassini mission since 2004

(Teanby *et al.* 2012, Vinatier *et al.* 2015). Ground-based telescopes miss out in recording the north-south asymmetry at short wavelengths where adaptive optics does not work yet. Cassini missed the last reversal that occurred around 2002, but may just catch the next one at the end of its mission. Cassini greatly excels in spatial resolution and complete phase angle coverage. Titan's consistent phase angle seen from HST and HST's photometric stability have advantages in detecting small seasonal variations.

HST imaging in a few filters recorded the seasonal variation well (Lorenz *et al.* 1997, 1999, 2001, 2004, 2006). A spectrally superior coverage comes from the Space Telescope Imaging Spectrograph (STIS) at HST that offers observations of 1024 wavelengths simultaneously, a wealth of spectral information. Methane spectroscopy allows probing many atmospheric levels. STIS records spatial information along the slit in a single exposure, and multiple offsets of the slit allow sampling of the second spatial dimension. Such data sets were taken in five years. They provide a four-dimensional record of Titan's seasonal change, one spectral dimension, one temporal dimension, and two spatial dimensions: one for latitudinal sampling and one for the center-to-limb variation of reflectivity. These data sets are the topic of this work.

In the following section we describe the data and our method of obtaining calibrated image cubes. Section 3 present a principal component analysis of the full data set. Section 4 explains the observed spectral signatures with radiative transfer modeling. Section 5 fits the observed latitudinal and temporal signatures with a seasonal model. Section 6 summarizes our work.

2. Data reduction

2.1 Observations

HST took images cubes of Titan with STIS in five years between 1997 and 2004: 1997,

1999, 2000, 2002, and 2004. In some years, multiple images cubes were taken within one orbit of Titan around Saturn. We picked the closest one observing Titan's trailing hemisphere. The probed northern seasons were early fall to early winter. The last observation occurred six months before Cassini arrived at Saturn. The G750L grating provided wavelengths between 530 and 1020 nm at 0.49 nm/pixel over 1024 pixels, of which the central ~1010 pixels gave useful data. The spatial sampling was 0.05 arc-sec/pixel along the slit, providing up to 17 pixels across the disk of Titan. The CCD can capture 1024 spatial pixels, but they are generally only partially saved. We used the central 100 spatial pixels to include plenty of sky background data. Spatial sampling perpendicular to the slit was accomplished through multiple exposures with slight positional offsets spaced by ~3 minutes. The successive offset for the five data sets was -0.125, 0.05, -0.05, 0.1, and -0.05 arc-sec, respectively, where positive offsets indicate a motion toward the evening hemisphere. The five data sets include between 3 and 19 different slit positions each.

Table 1 lists the basic observational parameters. Included is Titan's season with winter solstice corresponding to $L_s=270^\circ$. The rotation of Titan during each data set was less than $\sim 1^\circ$ and thus negligible. The median exposure level on Titan was about 1500 electrons per pixel, corresponding to a signal-to-noise ratio near 40. The principal investigators for these programs were Mark Lemmon (GO 7321, 9385 and 9745), Caitlin Griffith (GO 8229, year 1999), and Eliot Young (GO 8580, year 2000). Fig. 1 shows the central parts of the nine Titan images for the observations of 2002, including the flatfield taken afterwards. Fig. 2 shows the slit locations on Titan's disk according to our calibration, as will be explained in Section 2.8.

[Table 1 approximately here]

[Fig. 1 approximately here]

[Fig. 2 approximately here]

2.2 Raw images

We used the standard calibration pipeline by the Space Telescope Science Institute (STScI). This includes bias subtraction, flatfielding, and linearity correction (Ely *et al.*, 2011). These images are the basis for our further calibrations. We flagged ~50 pixels that had consistently low or high data numbers. An automated routine also found about 13,000 pixels on Titan or nearby that had high data numbers on a single exposure, most likely due to cosmic ray hits. We replaced these “bad” data numbers using linear interpolation between adjacent “good” data numbers.

2.3 Distortion correction

In STIS exposures, the spectral and spatial directions are not perfectly aligned with the column and row directions of the CCD, respectively. Furthermore, the wavelength is not a linear function of wavelength, but has quadratic and cubic terms. We rectified all exposures using the parameters from STScI (McGrath *et al.*, 1998), except for the tilt between the spectral direction and the CCD row axis, which was based on our measurements using flatfields taken right after the Titan exposures. The flatfields display dark streaks due to locations of decreased slit width, and the tilt of the streaks, about 0.3 pixels over the 1024 pixel extent, was accurately measured.

2.4 CCD fringes

Toward the longer wavelengths, STIS exposures display significant fringing as recorded in flatfields (bottom of Fig. 1) with intensity variations of up to 30 % peak-to-peak. We averaged each flatfield along columns and smoothed it spectrally by up to 30 pixels, which is larger than the spacing of fringes. We then divided the original flatfield by the smoothed flatfield, which created a fringe-flatfield for each observing date. Division by these fringe-flatfields reduced the fringes in the Titan spectra. A comparison of albedo spectra (cf. Section 2.11) yielded that the fringes were best reduced by increasing the amplitude of the fringes by 25 % at wavelength below 960 nm and then linearly increasing to 45 % at 1020 nm. The original flatfields recorded

the fringes with muted amplitudes due to scattering of the CCD discussed in Section 2.6.

2.5 Charge transfer efficiency

The charge transfer efficiency in STIS exposures is dependent on the exposure level (Goudfrooij and Kimble 2002, Goudfrooij *et al.*, 2006). Based on Karkoschka and Tomasko (2009) using a similar STIS image cube of Uranus, we adopted that 10 % of the signal was lost for exposures with levels of 30 electrons/pixel, that the loss is proportional to the exposure level to the power -0.4, and that the spatial deposition of charge toward lower columns was according to an exponential decay of $1/e$ every 20 pixels. We deconvolved the images using the Wiener method, which puts the lost charge back to its origin. The initial intensity asymmetry in the sky background on both sides of Titan vanished after deconvolution.

2.6 Scattered light

The STIS CCD is a backside illuminated chip, which creates wide halos of scattered light, especially longward of 750 nm, smoothing out spectral and spatial features. For example, at 905 nm wavelength, the fractional energy in the halo is ~30 % (Quijano et al., 2007). We used the same deconvolution method as in Karkoschka and Tomasko (2009) to put all scattered light back to its origin. Signal levels in the sky on both sides of Titan got strongly reduced, to levels roughly consistent with telescope diffraction. The scattered light is up to ~10 times larger than typical albedo variations on Titan. Thus accurate deconvolution of scattered light is essential. Our method was sufficient for detecting variations as small as 0.3 % within STIS data, but does not allow cross calibration with other data sets to similar levels, which is inherently difficult.

2.7 Spectral calibration

For each exposure, we co-added all data numbers along columns to obtain one-dimensional

spectra. We used the solar Fraunhofer sodium D and hydrogen H- α lines (cf. Fig. 1) to calibrate the wavelength scale in each exposure. We employed an automated routine that accurately locates the line using the whole line profile. We averaged data for both lines with weights of 0.85 for the strong hydrogen and 0.15 for the weak sodium line. All measurements are displayed in Fig. 3 (top). The lines can shift by 3 pixels between observing sessions, but only by a fraction of a pixel within each observing session. Variations are close to linear with shifts of 0.015 pixels per exposure number root-mean-square (rms), which is a measure of flexure within the instrument. Our adopted straight lines in Fig. 3 differ from the measurements by 0.05 pixels rms, which is probably our measurement precision. This corresponds to 0.025 nm. We used our fits and the dispersion of 0.48836 nm/pixel provided by STScI to calibrate the wavelength scale.

[Fig. 3 approximately here]

The observations taken with the wide slit (~ 2 pixels wide in 1997, 2002, 2004) had a poorer spectral resolution than the ones taken with the narrow slit (~ 1 pixel in 1999, 2000), which is evident when measuring the depths of the solar lines. Additionally, observations taken near the center of Titan with a fully illuminated slit had a poorer spectral resolution than those near Titan's limb, where only part of the slit was significantly illuminated, especially for the wide slit. We convolved all spectra by 3-point averages with a weighing of the three pixels of x , $1-2x$, x , where we adjusted x for each slit width and location on Titan to produce spectra of identical resolution, about 1 nm. The adjustment was small with typically $|x| < 0.1$. This allowed accurate removal of solar features in the division by a solar spectrum of 1 nm spectral resolution.

2.8 Spatial calibration

For the spatial calibration, we co-added all data in each row to create one spatial profile for each exposure. We located Titan's limb by finding the profile's steepest gradients using cubic interpolation between data points (solid dots in the bottom panel of Fig. 3). The half-way point

between both measurements is shown by open circles. Linear fits to these data give shifts of 0.018 pixels per exposure number rms, which is similar to the instrument flexure in the spectral direction (0.015). These shifts could also be due to a tracking error of 0.0009 arc-sec per exposure number rms. The rms offset between open circles and linear fits is 0.035 pixels (0.0018 arc-sec), indicating our measurement precision. We adopted the linear fits as our navigation along the slit.

For the navigation perpendicular to the slit, we first adopted the commanded offset from one exposure to the next (0.05, 0.1, or 0.125 arc-sec). In order to find Titan's center, we used the distance between the curves and central lines of Fig. 3. The distance as function of exposure number could be fitted by a quadratic function with a small fourth-order term added, to 0.014 pixels rms (0.0007 arc-sec), except for the last two exposures in 2000 where the offset is ~40 times the rms value, maybe due to a tracking error (cf. Fig. 3). For those two exposures we used estimates from our best-fit curve to adjust the commanded offset by 0.026 and 0.036 arc-sec, respectively. The maximum of the distance function is our adopted navigation for Titan's center.

We refined this initial navigation in both axes with three improvements. First, Titan's sharp limbs in strong methane bands provides superior navigation. Thus, we co-added only wavelengths with methane absorption coefficients larger than 0.5 (km-am)^{-1} . This modification changed our navigation by 0.06 pixels rms, corresponding to 0.003 arc-sec rms.

Second, at non-zero phase angles, automated navigation is typically biased toward the bright limb due to uneven illumination. Simulations with synthetic images indicated that our routine is biased by 1/6 of the distance between sub-solar and sub-Earth points, which we adopted for our correction. This modification changed our navigation by 0.002 arc-sec rms.

Third, our north-south navigation is also influenced by asymmetries on Titan's disk. Simulations using our routine suggested adjustments of 0.002 arc-sec rms which we adopted. We estimate that this value is the accuracy of our navigation. Since the largest intensity gradients in

our data up to 1 pixel inside of Titan's limb are 25 %/pixel, the maximum photometric error due to imperfect navigation is ~ 1 %, and but much less closer to Titan's center.

The orientation of the slit is provided by STScI (Fig. 2). We resampled all data using cubic interpolation to a constant wavelength scale at 0.4 nm/pixel and a constant spatial scale of 0.06 Titan radii per pixel with the central column aligned with Titan's central meridian.

2.9 Telescope diffraction

HST has a point spread functions (PSF) with a narrow, ~ 0.1 arc-sec core, but ~ 25 % of the signal is diffracted by more than 0.2 arc-sec, which is about half of Titan's radius. We deconvolved the wings of the PSF with the Wiener method using monochromatic PSFs from the TinyTim software by STScI (Krist, 2004) every 40 nm wavelength and linear interpolation in between. We smeared the PSFs perpendicular to the slit according to the slit width, and then scaled and rotated them in the same way as our Titan image cubes. Our deconvolved data set has a PSF with a full width at half maximum (FWHM) of 0.12 arc-sec. This value is similar to that of the original PSF, but now the core contains 100 % of the signal instead of ~ 75 %. Deconvolution needs the whole image of Titan which was not always observed. We estimated the missing part by interpolation along concentric circles, linear interpolation in position angle.

2.10 Albedo calibration

Our albedo calibration uses the solar flux spectrum by Colina *et al.* (1996) and the conversion between data number and flux for each wavelength adopted by Karkoschka and Tomasko (2009, their Fig. 5) for a similar STIS image cube of Uranus. This calibration applies for the first, fourth and fifth image cube, which used the same slit width as the Uranus data. For the other two data sets with the narrower slit we determined additional calibration factors from the flatfields. This calibration is different from the STScI calibration because of different

methods in deconvolving the significant scattered light of the CCD.

We adjusted the absolute calibration using the ground based photometry of Titan in the y filter by Lockwood and Thompson (2009), which includes adjustment to constant distance from sun and Earth. For comparison, we also used the geometric albedo spectra of Titan provided by Karkoschka (1994, 1998). The y filter is centered on 551 nm with a FWHM of 23 nm. Lockwood and Thompson (2009) give a phase coefficient of Titan in the y band of 0.004 mag/deg and corrected their observations to zero phase angle. We did the same, assuming a constant coefficient with wavelength, which increased reflectivities by up to 1.2 %. For each image cube and each wavelength, we co-added all data spatially to calculate geometric albedos. Then we convolved all spectra with the transmission curve of the y filter (Table 5 in Lockwood and Thompson 2009) to calculate y -filter albedos.

In order to plot albedos on the magnitude scale of Fig. 4, we adjusted three calibration constants to get the best match with Lockwood's data, two constants for the narrow and wide slit and one for the spectra of Karkoschka (1994, 1998). The three constants fix the geometric albedo in the y band, and the same calibration factor is adopted for the whole spectrum. Fig. 4 shows that all our data is consistent within Lockwood's error bars, which correspond to typically 0.3 % in albedo. The rms deviation between their and the STIS data points is 0.2 %. The temporal variation in STIS data is even smoother than in Lockwood's data. We estimate that our absolute calibration is good to 4 %, and our relative calibration within the data set to 0.2 %.

[Fig. 4 approximately here]

Fig. 5 shows a comparison of the average geometric albedo spectrum from this work with the ground-based spectrum by Karkoschka (1998). In the visible, there is good agreement. Toward infrared wavelengths our spectrum is consistently higher, similar to brightening observed between 1993 and 1995 (Karkoschka 1998).

[Fig. 5 approximately here]

2.11 Spectral reduction

Titan's spectrum is influenced smooth spectral variations and the steep methane spectrum. Smooth variations include Rayleigh scattering, aerosol optical depth, aerosol optical parameters, and Titan's surface albedo. In our spectral range, smooth variations are sampled sufficiently well at 5-10 wavelengths with cubic or spline interpolation in between. Likewise, the change of reflectivity with the methane absorption coefficient is sampled sufficiently well at 5-10 methane strengths. We divided our spectral range into eight wavelength regions roughly centered on a methane band each (Fig. 5), and we divided methane absorption coefficients into seven regions centered on coefficients that are spaced by factors of $\sqrt{10}$ based on coefficients for 100 K temperature by Karkoschka and Tomasko (2010).

This divides our spectral information into 25 spectral bands. Each spectral band represents a specific range of wavelength and methane absorption coefficient. Each band gives the average of some 40 original data points, which significantly decreases noise. Our averaging used weights and correction factors to the ~40 data points in such a way that their average represents Titan's reflectivity for the nominal wavelength and methane absorption coefficient. We corrected for the curvature of Titan's spectrum since it affects reflectivity averages by about 1 %. Our reduction from 1024 to 25 spectral data points retains all essential information about Titan. Spectral bands with the same wavelength but different methane strengths and others with the opposite way simplify the distinction between methane and smooth spectral variations (Sections 3-5). While each wavelength has its methane absorption coefficient, different spectral bands with the same central wavelength have different methane absorption coefficients.

2.12 Titan's surface

At the longest wavelengths and smallest methane absorption coefficients, our images probe

Titan's surface. We took a surface map of Titan (# PIA 14908) made from Cassini's Imaging Surface Subsystem (ISS) camera near 940 nm wavelength, smoothed it to our spatial resolution, and projected it according to our sub-Earth longitudes and latitudes (Fig. 6, right side). Our surface features correlate with the features seen by ISS. For each spectral band, we did a linear regression of our reflectivity values with the general limb darkening subtracted versus the data numbers in the ISS map. We averaged data from our five observing dates with weights according to the total signal received from Titan. The slope of each linear fit indicates how much Titan's geometric albedo changes with surface albedo between the darkest and brightest spot in the ISS map since the map was normalized between 0 and 1. This is shown as the dashed curve in Fig. 5. Our curve confirms that Titan's surface can be easily probed at the longest wavelengths and smallest methane strengths. Our curve is noisy because of limited signal from the surface.

[Fig. 6 approximately here]

We used the projected ISS maps and the linear fit for each wavelength to correct all our reflectivity data to a constant average surface albedo, which removed Titan's surface features from our images. This process was not perfect, but reduced features by a factor of three at which point they were close to negligible. Remaining features may be due to imperfections of the ISS map, which has intensity discontinuities at boundaries of original ISS images.

2.13 Spatial reduction

Our original data sample up to 17 latitudes along each slit. We divided Titan's globe into 10 latitude regions so that each region contains one or two such data points. The 10 latitude regions are divided by the latitude circles every 10° from 60° South to 20° North (cf. Fig. 3).

The spatial resolution of HST is only four times smaller than Titan's radius, so that the center-to-limb variation of reflectivity within a latitude region can be approximated well with simple functions. We used the linear limb darkening function:

$$I/F = S \mu_0 / (\mu + \mu_0) + L \mu_0 \quad (1)$$

where I/F is the reflectivity, μ_0 and μ are the cosines of the angles of incidence and emission, respectively, and S and L are two fitted parameters. For $S = 0$ Eq. (1) becomes the Lambert Law (Minnaert exponent 1), and for $L = 0$ the Lommel Seeliger Law (Minnaert exponent 0.5).

We calculated scattering geometries based on the altitude where the aerosol optical depth reaches 0.5 from Tomasko *et al.* (2008). This means that we used an optical radius of Titan between 2600 and 2800 km with the radius increasing toward shorter wavelengths.

We sampled our linear limb darkening function at $\mu = 0.6$ and 0.8 since this is within the typical range of observations of μ between about 0.5 and 0.9. The lower limit of 0.5 comes from our exclusion of data points within one pixel of the limb. We call the reflectivity ratio $I/F(\mu=0.8) / I/F(\mu=0.6)$ the limb darkening ratio; the larger the ratio, the stronger the limb darkening. In every wavelength range, the limb darkening ratio decreases with increasing methane absorption since $I/F(\mu=0.8)$ probes deeper into Titan's atmosphere and is thus more affected by methane absorption. Fig. 5 shows the strong correlation between albedo and limb darkening.

In summary, we reduced the data from about 1 million original data points to 2500 data points, 25 spectral bands, 10 latitudes, two center-to-limb locations, and five observing dates.

3. Principal component analysis

3.1 Method

The principal component analysis is a useful tool to understand the main features in a data set if the data set is sufficiently complex so that other methods may miss some features, and if the variations are sufficiently small so that the superposition of different effects is close to linear. Both conditions are met in our data set.

The principal component analysis has the goal of splitting a function of several parameters

into a product of two functions A and B where the first function depends on some parameters and the other function depends on the remaining parameters. Both functions are typically much simpler than the original one so that the characteristics of the data can be understood. The functions are defined so that their product is as close as possible to the original one. Typically, the sum of the squares of all residuals is minimized. In the second step, the residuals are approximated by a product of two new functions as well as possible. In the third step, the same is done for the remaining residuals, etc. Typically, the average with respect to the second set of parameters is subtracted from the original function which gives averages of zero for the functions B , which are then normalized. The solution is unique except for factors of -1 for each pair of functions. The functions A have the unit of the original function, while the functions B have scalar values. The procedure of finding the functions is facilitated by existing software packages.

In our implementation, the first set of parameters represent different observations of the same atmospheric structure: wavelength, methane strength, and viewing angle. The atmospheric structure depends on the remaining parameters: latitude and time. Thus we expand our data set in the following way:

$$I/F(\lambda, \kappa, \mu, \varphi, t) = C(\lambda, \kappa, \mu) + \sum_i A_i(\lambda, \kappa, \mu) B_i(\varphi, t) \quad (2)$$

where λ is the spectral band's central wavelength, κ the methane absorption coefficient, φ the latitude on Titan, t the observing date, C the spatially and temporally averaged reflectivity, and A_i and B_i the principal component functions, and $i=1,2,\dots$ denoting the first, second principal component, etc. The functions A_i describes the spectral and center-to-limb dependence of reflectivity for a certain physical change of the atmosphere relative to its average state described by the parameter C . A_1 describes the most significant physical change observed, A_2 the second most significant, etc. The functions B_i describe the size of the physical change for each location and time, normalized to the rms change over the whole data set. We call individual values of the functions A_i *amplitudes* since they indicate the rms variation of reflectivity over the whole data

set for each principal component. For B_i we used the term *values* since they indicate the change for a certain location and time relative to the rms variation for each principal component.

We assigned weights to our 2500 data points according to the observed area on Titan's disk of each latitude section and reduced weights for the shortest and longest wavelengths where the spectrograph has low sensitivity. The weighted average difference in reflectivity between I/F and C is 0.011. Its square we call the 100 % variance for reference.

We used iterations to find the first five principal components. They explain 83.8 %, 11.8 %, 2.6 %, 0.9 %, and 0.4 % of the variance, respectively, while the remaining 45 components share the remaining 0.5 % of the variance. Since the data set contains 50 combinations of λ, κ, μ and 50 combinations of ϕ, t , 50 principal components are needed to fit the data perfectly. The fifth principal component has its highest amplitudes A_5 at the extreme wavelengths, where noise can be seen in Fig. 6. This suggests that the fifth and further components describe mostly noise. The total noise corresponds to 1 % of the variance and thus a reflectivity precision of 0.001.

The fourth principal component has its two highest amplitudes A_4 at the 890 and 793 nm continuum bands, respectively, and the next highest amplitudes at the next methane absorption coefficients of both bands. This is exactly where the surface features of Titan are most visible (Fig. 6). We do not consider it further since we focus on Titan's atmosphere in this work.

The first three principal component data are the main results of this work and displayed in Fig. 7, showing A_1 through A_3 ordered first with methane absorption coefficient and then with spectral band. Fig. 8 shows A_1 and A_2 ordered the opposite way. Values B_1 through B_3 ordered first with latitude and then with observing date are displayed in Fig. 9, and B_1 and B_2 ordered in the in opposite way in Fig. 10. The contributions of the first and second principal components to the reflectivity across Titan's disk for 1999 and 2002 are displayed at the bottom of Fig. 6. The amplitudes A_1 and A_2 are listed in Table 2, the values B_1 in Table 3, and B_2 in Table 4.

[Figs. 7-10 approximately here]

[Tables 2-4 approximately here]

3.2 Interpretation

The first and second principal components in Fig. 10 display north-south asymmetries that change with time and are thus related to Titan's seasonally changing north-south asymmetry, described by Lorenz *et al.* (1997). The fact that two principal components explain essentially all observed atmospheric variations is interesting. It suggests that the north-south asymmetry has two different components that together explain essentially all recorded variations.

The functions Bi describe changes as function of latitude and time. For now we only consider the plotted data points in Fig. 10, the curves will become important in Section 5. Both principal components show a strong north-south asymmetry in the beginning of our observing period (1997). By the end of the period (2004), the first principal component reached symmetry between north and south, while the second component reached symmetry already around 2001. Note that Titan's northern winter solstice occurred in late 2002, roughly half way between the symmetry dates of both components. Thus, the components are phase delayed with respect to seasons by a little more than 90° for the first and second principal component, and a little less than 90° for the second one. The curves in Fig. 10 show a dip at the tropics for the first component but a bulge for the second component. The conditions at tropical latitudes are not close to Titan's average. For the second principal component, tropical latitudes have a condition close to those of southern latitudes before the contrast reversal. An enhanced haze around the equator was detected by Cassini ISS and VIMS with high spatial resolution (Kok *et al.* 2010) that probably corresponds to the feature seen in the second principal component as we will see later. The strongest latitudinal gradients occur at mid latitudes, while beyond 50° South, the curves get more shallow. All curves are smooth near the scale of spatial resolution. At smaller scales, Titan's north-south asymmetry has a relatively sharp edge (Kok *et al.* 2010), and at even smaller

scales of $\sim 1^\circ$ in latitude Cassini ISS has detected intricate structure of narrow strips of very low contrast (Porco *et al.* 2005). In our data, the strongest small-scale feature, a little dip at 25° South in 1997, is probably noise due to low data volume of the 1997 observations.

Fig. 9 shows the same data with a little different emphasis. At high southern latitudes, the first principal component was probably close to its maximum value at the first observation and then close to zero at the last observation. Values decreased toward lower latitudes and at 5° North, there was essentially no change, with a constant negative value as noted above. The slightly rugged curve at 5° North has a peak-to-peak variations of about 0.4. Multiplied by the typical size of A1 values of around 0.008 yields a rugged reflectivity of about 0.003, which is close to the expected photometric stability and thus not a significant effect. For the second principal component, the high southern latitudes show small positive values early on and then very negative values after 2001. At 5° South, the atmosphere was stationary at a positive value. At northern latitudes, values increased with almost constant speed.

The functions A1 and A2 describe the spectral shape of reflectivity and center-to-limb variations for the most and second most significant physical change on Titan. For the first principal component, amplitudes are essentially zero at the spectral bands with the shortest wavelengths and also at the strongest methane absorption coefficient observed in the 890 nm band (Fig. 8). This indicates that the physical change described by the first component is probably located at lower altitudes, where light is absorbed either by dark aerosols at short wavelengths, or by methane gas in methane bands. The center-to-limb variation also indicates a low altitude location. Everywhere, amplitudes are larger at $\mu = 0.8$ (solid dots) that probes deeper into the atmosphere than at $\mu = 0.6$ (open circles). This is especially true at weak methane absorptions at the longer wavelengths that probe the lower atmosphere. Essentially all amplitudes of the first principal component are positive indicating a consistent effect.

The situation is very different for the second principal component. The amplitudes are

negative for wavelengths below 700 nm and generally positive beyond (Fig. 8). The physical change associated with the second principal component acts in different directions at short versus long wavelengths. Almost all data points indicate more positive amplitudes for larger methane absorption coefficients that probe the upper atmosphere. The center-to-limb variation goes the same way everywhere. The open circles probing higher altitudes are above the solid dots probing lower altitudes further suggesting that the second principal component is rooted at high altitudes. Similar conclusions can be drawn from Fig. 7 displaying the same data in different order.

4. Radiative transfer modeling

4.1 Altitude determination

We based our radiative transfer calculation on the method and model by Doose *et al.* (2015), the revised DISR haze model. It provides the optical depth, single scattering albedo and phase function of the aerosols as function of wavelength and altitude. The model's haze optical depth has a scale height of around 50 km above ~100 km altitude and then gradually transitions into a roughly linear increase of optical depth with decreasing altitude, corresponding to roughly constant extinction coefficient (opacity). Since the model was based on data taken during the descent of the Huygens probe, it is valid for a latitude of -10° in January 2005.

Our data constrain the vertical optical depth profile of the haze relative to the methane profile, but not both independently. Since we expect that variations in the haze strongly dominate those in the methane profile, we assumed the methane profile to be constant and investigated only haze variations.

To compare radiative transfer models with observations, we selected 22 spectral bands for the $\mu = 0.8$ scattering geometry. The $\mu = 0.6$ data are neglected for now since they are more affected by the third principal component. We did not consider the three spectral bands that are

most sensitive to the surface features, the continuum data at the 793 and 890 nm spectral bands and the next methane absorption coefficient ($0.10 \text{ (km-am)}^{-1}$) at 890 nm because elimination of surface features was not perfect. With these 22 data points, the first and second principal components together capture 99 % of the variance, so that further components can be neglected.

These 22 data points have an average wavelength of 780 nm and a standard deviation of 80 nm. Thus, our data can constrain optical parameters at 780 nm and can constrain significant variations over an interval of 80 nm. The measured amplitudes of the two principal components are too small to do more, such as determining a curvature in an optical parameter.

At first we studied how variations of the haze opacity influence model reflectivities. Within a selected altitude range, all haze opacities (haze extinction coefficients) were multiplied by the same factor, which we call the opacity factor, while opacities were left unchanged outside the selected altitude range. The 890 nm data points are best suitable for this purpose since they include the spectral bands that probe the lowest and the highest altitudes in our data.

Fig. 11 shows three models with the opacity increased with respect to the revised DISR haze model at 890 nm below 60, 80, and 100 km altitude (top panel left to right). The solid curves are from the models, plotting the difference of the model with larger opacity minus the reference model. The solid dots are the observed amplitudes A_1 (first principal component). The first two dots are plotted in smaller size since they are not part of the selected 22 spectral bands and thus do not influence the fits. Likewise, the dotted curves and open circles are model and observed data for the $\mu = 0.6$ scattering geometry that are not used for fits, but still should fit roughly. In each panel, the opacity factor was adjusted to minimize least-square residuals. For the second panel at top, the haze opacity within the 0-80 km altitude region was multiplied by 1.46. Larger or smaller opacity factors move the model curves proportionally away or closer to the zero level, but do not change the shape. The 0-80 km model provides a good fit to the data with residuals below 0.001. The curve for the 0-60 km case is too steep, and for the 0-100 km

case to shallow.

[Fig. 11 approximately here]

We also varied the bottom altitude limit of the opacity change and found always good fits whenever the top limit was near 80 km. The data are not very sensitive to the bottom limit. However, observed values of $B1$ of -3 or smaller require the removal of more haze than there is in a shallow layer such as 60-80 km. Thus, our nominal altitude range for the first principal component is 0-80 km.

Fig. 11 shows a similar investigation for the $A2$ amplitudes. In this case, we changed the haze opacity above 200, 150, and 100 km (bottom panel left to right). The first case has model curves too steep, the last case too shallow. The middle case with opacities changed above 150 km provides the best fit and thus is our nominal case for the second principal component. We tested extra models with the altitude range limited at various top levels and found little sensitivity as long as the top limit was above 200 km, mostly because optical depths of Titan's aerosols above 200 km altitude are only on the order of 0.1 at 890 nm wavelength. Our models with sharp boundaries at 80 or 150 km altitude are rough large-scale approximations, while real altitude profiles may be smooth and more complicated on smaller scales.

In our nominal cases, the data points not used for fitting are fairly close to the model curves. For the first principal component, open circles are consistently slightly below the dashed curve. This is probably due to the radiative transfer code that assumes Titan's atmospheric layers to be plane parallel. In reality, the light beam for a $\mu = 0.6$ geometry has the first and last scattering roughly at 120 km altitude. At the point where the beam reaches 80 km altitude, the surface has curved away and the geometry has changed to $\mu = 0.58$. Thus, the altitude region of change should be calculated with $\mu < 0.58$ but the simple code for a flat Titan uses 0.6 for all altitudes. It underestimates the difference with respect to the $\mu = 0.8$ geometry.

The third principal component has values of about twice the noise which is insufficient to

obtain a significant result, but indicates that something other than noise probably contributes. The large $A3$ amplitudes for $\mu = 0.6$ compared to $\mu = 0.8$ (Fig. 7) cannot be reproduced in radiative transfer models, suggesting that it does not correspond to a change on Titan. Its spectral dependence seems to be correlated with that of the first principal component indicating that it may be some non-linearity effect associated with the first component.

Our radiative transfer calculations showed that the linearity of reflectivity according to Eq. (1) was almost valid. For zero phase angle Eq. (1) means that the reflectivity is linear in μ , but there was generally a small negative curvature. This means that reflectivity values at $\mu = 0.8$ are slightly overestimated in our fit if the observations do not include this scattering geometry but only provide a linear extrapolation from smaller values of μ . This is the case for the -65° latitude region at the first two observations dates, for -55° also at the first one, and for the 25° latitude region at the last four dates. The overestimation implies that the principal component analysis cannot fit the data perfectly and needs an extra component to describe these systematic effects for the strongest component(s). Based on our implementation, one expects negative $B3$ values for the latitudes listed above. This is roughly true (Fig. 9). Thus, the third principal component is partially due to the linearity approximation of Eq. (1), and otherwise noise or other minor systematic effects. We estimate that this effect caused overestimation of the $B1$ values by about 10 % for the latitudes listed above, which is barely significant since both extreme latitude regions have results of lower quality anyway.

4.2 Physical parameter determination

In Fig. 8 we display similar models as in Fig. 11, but display all spectral bands. With the added data points, the opacity factor for the lowest residual is 1.33, somewhat smaller than the 1.46 obtained above for the 890 nm band. Across all spectral bands, the model catches the main features of the data reasonably well. The residuals are slightly reduced if the opacity factor

increases with wavelength as would be expected when aerosols increase in size, not just in numbers. Thus, the first principal component may characterize an increase of aerosol sizes that directly causes an increase of opacity. Our data are not good enough to clearly distinguish the contributions from increased numbers of aerosols and increased sizes.

In Fig. 12, we display a model with the same altitude ranges as before, but with a changed aerosol phase function instead of opacity: adding f times an isotropic phase function to the original one multiplied by $1 - f$. A spectrally constant f did not provide the best fit for the first principal component, but a linear trend accomplished it when using $f = 0.057$ at 700 nm and $f = 0.086$ at 860 nm. For the second principal component, our change of phase function is completely inconsistent with the data.

[Fig. 12 approximately here]

Fig. 13 displays a model for a change of single scattering albedo at the same altitude ranges as before. For both principal components, such models can be ruled out easily. Since the single scattering albedo of the DISR haze model reaches values close to unity, we reduced it for our changed values, but still plot the reflectivity difference of brighter minus darker model. This figure emphasizes the power of spectroscopic data. Imaging data is often constrained to the continuum and the center of a methane band, for example the first and last data points of the 890 nm spectral region. With those data points, the first principal component can be fit well with a change of single scattering albedo. But the data points in between are critical to judge the model.

[Fig. 13 approximately here]

4.3 Discussion

The approximate altitude regions for the first and second principal components are 0-80 km and 150 km to the top of the atmosphere, respectively. Both can be explained by a change of haze opacity. The first one can also be fit by a change of phase function, and a change increasing

with wavelength. The small residuals of the two possible cases for the first principal component behave the opposite way. For the opacity case, the curves are above the data at middle bands (around 727 nm) and below the data at the spectral ends. For the phase function case, the opposite is true. A combined case with both parameters changing by about half as much as in Fig. 11 and 12 fits the data even better. It is conceivable that as the aerosols fall through the altitude region around 80 km, they change due to condensation of gases. The condensation could change the aerosol size, the opacity, and the phase function of aerosols. Several gases are expected to condense between 70 and 90 km altitude. Lavvas *et al.* (2011) argued that HCN dominates and that aerosols in the 30-80 km altitude range should be strongly coated by HCN. This altitude range fits the range determined for the first principal component since the data are sensitive to the top altitude but not to the bottom altitude of the layer.

It makes sense that for aerosol at low altitudes, opacities and phase functions have similar effects for observed reflectivities. In both cases, more or less light is reflected back to the upper atmosphere, by a variation of haze opacity or back scattering part of the phase function.

The combination of the first two principal components represents Titan's north-south asymmetry that switches back and forth every Titan year. It was detected by Voyager (Smith *et al.* 1981, 1982) and refined by HST (Lorenz *et al.* 1997, 1999, 2001, 2004, 2006), Cassini ISS imaging (e.g. Porco *et al.* 2005), and Cassini VIMS observations (e.g. Brown *et al.* 2006). While its latitudinal structure has been known well, its interpretation and vertical location has been difficult to determine. Our STIS data probing multiple methane absorption strengths within the same spectral bands are among the best current observations for that purpose.

Cassini data have provided excellent constraints on reflectivity *ratios* over large temporal, latitudinal, and spectral ranges (e.g. Penteado *et al.* 2010), but detection of small variations in *absolute* reflectivities have been hampered by the constantly changing geometry. Ground-based observations have a constantly low phase angle, but a variable Earth's atmosphere. HST

combines the advantages of both kinds of observations yielding to a photometric calibration of 0.2 % between the five STIS data sets that allowed accurate characterization of temporal change.

The first principal components have been difficult to distinguish from each other because their spatial and temporal variations are somewhat similar. Lorenz *et al.* (1999) noted a time dependence of the north-south asymmetry with wavelength that became clearer later on (Lorenz *et al.* 2001) based on imaging in about eight filters. It indicated that high and low altitudes do not change in tandem. Ground-based studies using adaptive optics systems also indicated an earlier reversal of the north-south asymmetry at high altitudes (~130 km) compared to altitudes around 50 km (Hirtzig *et al.* 2006). These studies of the hemispherical asymmetry ignored latitudinal variations within each hemisphere. Our spectroscopic data and more comprehensive analysis showed that both components are separated and have their own characteristics such as the latitudinal profile as function of time.

An explanation for the optical depth change at high altitudes is the transfer of aerosols by atmospheric dynamics. Perhaps, there is a contribution from variable speeds of coagulation changing aerosol sizes, also influenced by atmospheric dynamics. Optical depths at our wavelengths dependent strongly on aerosol sizes.

Our second principal component probing mostly altitudes just above 150 km has a north-south asymmetry that is opposite to the measurements of Titan's shadow in 1995 that suggested that aerosols around 300 km altitude are about half the size at high southern latitudes compared to northern latitudes (Karkoschka and Lorenz 1996). This suggests that our results cannot be extrapolated to altitudes 3-4 scale heights higher than the region our data probe.

5. Time variability modeling

5.1 Seasonal model

The functions Bi describe a scale factor for the characteristic change of each principal component for various times and latitudes. Figs. 9 and 10 and Tables 3 and 4 show and list these functions for five dates and 10 latitudes. In this section, we assume that all variations are purely seasonal, and that the reflectivity at each latitude and scattering geometry varies with time as a sine curve with the period of Titan's year (29.46 years). We suspect that a major part of the observed variations are seasonal, but probably not 100 %. Light curves in blue and green light are similar to sine curves (Lockwood and Thompson 2009), but they are not perfectly periodic. We approximate the temporal variation of the functions $B1$ and $B2$ by the following seasonal variation:

$$Bi(\phi, t) = Mi(\phi) + Di(\phi) \sin [(t - Ei(\phi)) 2\pi/29.46] \quad (3)$$

where Mi is the mean value, Di is the amplitude of the seasonal variation, Ei is the epoch (in decimal years) when values go through their annual mean, t is the date, and the index i indicates the first or second principal component. The parameters Mi , Di , and Ei are the three parameters for the sine curves. They are all functions of latitude.

The temporal range of the observations, almost a Titan season, is insufficient to constrain all three parameters of sine curves. This is especially the case since the three observing sessions with a large number of slit positions and thus high quality data cover only a period of 3 years, only 10 % of a Titan year. Thus we needed additional constraints for unique solutions. We assumed that both hemispheres on Titan act symmetrically except for a phase shift of 180° , half a Titan year. This provided adequate constraints for latitudes within 30° of the Equator but no additional constraints at higher latitudes. Thus, beyond $\pm 30^\circ$, we assigned the parameter Ei based on measured values at low latitudes, at least for the second principal component where this assumption was consistent with the data. For the first principal component, residuals decreased significantly by increasing Ei by about a year for higher latitudes. Any further increase would not have reduced residuals significantly. Thus, our data suggest that for the first principal

component, high latitudes have a slightly delayed seasonal change compared to the tropics.

Our parameters of seasonal change are displayed in Fig. 14. As we noticed in Section 3, the phase of the second principal component is ahead relative to the first one. Seasonal amplitudes Di for both components increase almost linearly away from the Equator. The temporal mean Mi is different at low and high latitudes. Our model describes an approximation of the state of Titan for every time and all latitudes except close to the poles. The parameters describe the changes of Titan's haze that provide critical data for Global Circulation Models.

[Fig. 14 approximately here]

Fig. 10 displays the Bi values calculated from Eq. 3 as curves with the observations as dots. Most data are fit well by the curves. Large deviations occur only where little data exist, indicated by a small dot size in Fig. 10. The smallest dots indicate uncertainties five times larger as for the largest dots. The good fit means the seasonal model is consistent with the data, but the validity at other latitudes and times than observed has to be tested elsewhere.

5.2 Haze opacity factors

Section 4 showed physical parameter changes in Titan's atmosphere that correspond to the functions $A1$ and $A2$. Since they are multiplied by $B1$ or $B2$ in Eq. 2, they are appropriate wherever the values $B1$ or $B2$ increase by unity. If $B1$ or $B2$ increase by 2, the reflectivity change is twice as much, implying twice the change in the haze opacity if reflectivities go linear with haze opacity. Using radiative transfer models, we determined the relationships between $B1$ and $B2$ and opacity factors. They are almost but not perfectly linear (Table 5).

[Table 5 approximately here]

Our reference model is the DISR haze model valid for -10° latitude in early 2005. From Figs. 9 and 10, we estimated parameters $B1 = -1$ and $B2 = 0$ for this latitude and time. Thus, our mapping between opacity factors and $B1$ or $B2$ is anchored at these values. The parameter $B1$

refers to the opacity factor at altitude below 80 km, and $B2$ to altitudes above 150 km.

The opacity factors of Table 5 go over wide ranges. Both go almost to zero and go up over 2 ($B1$) and to about 1.5 ($B2$). This suggests that the aerosol opacity at the low and high altitudes undergoes large variations. Cassini observed large variations (e.g. Vinatier *et al.* 2015) that are roughly consistent with our HST data, although Cassini data catch variations on much smaller scales in altitude, latitude, and time.

Fig. 15 displays the relationship between opacity factors on the right side and the values of $B1$ and $B2$ on the left side. The seasonal model (Eq. 3) is plotted for a full Titan year. Tropical latitudes that were observed on both sides of the Equator are plotted as solid curves, observed latitudes further south as dashed curves, and the unobserved latitudes in the north as dotted curves. They are based on the assumption of the seasonal model that southern and northern latitudes behave symmetrically except for a two-season phase shift.

[Fig. 15 approximately here]

The characteristics of both principal components are evident in Fig. 15. The annual averages $M1$ do not vary much with latitude (top of Fig. 14). Thus, the top panel of Fig. 15 is almost symmetric in the vertical direction. On the other hand, $M2$ is quite dependent on latitude and thus the curves in the middle panel of Fig. 15 are quite asymmetric in the vertical direction. The epoch parameter $E2$ is constant with latitude, creating a figure symmetric in time (middle panel of Fig. 15). This is not the case for $E1$, which shows up as a horizontal shift of phasing between low (solid curves) and high latitudes (dashed and dotted curves). The earlier phasing of the second principal component with respect to the first one is also obvious.

The accuracy of the seasonal model can be estimated from the rugged variations in Fig. 9 with a size of about 0.5 for the values of $B1$ and $B2$. Fig. 10 suggests similar differences between observations (dots) and the seasonal model (curves), although larger dots for $B1$ differ typically by only about 0.2 from the curves, while some smaller dots for $B2$ differ by unity from the

curves. We conservatively estimate an accuracy of 0.5 for $B1$ and 1 for $B2$, which corresponds to an accuracy of 0.2 for opacity factors. However, we suspect that the opacity variations could be significantly smaller than in our model. At low altitudes, phase function variations may explain part of the observed variation. At high altitudes, lowering the boundary of change from 150 to 100 km would decrease the required opacity deviations from unity by a factor of two.

5.3 Discussion

Fig. 15 shows that near the 2009 spring equinox, the $B2$ values for the northern hemisphere cluster tightly near the maximum. Just south of the Equator, curves are spaced far apart but clustered somewhat further south. This means that the northern and southern latitudes are very roughly uniform with a relatively narrow transition region just south of the Equator. This is just what Voyager observed shortly after the previous spring equinox, a bright southern and a dark northern hemisphere with a transition region near 10° South (Smith *et al.* 1981, 1982). Since higher haze opacities correspond to darker reflectivities, Voyager images fit the seasonal model.

The variations observed by HST are consistent with ground-based photometry by Lockwood and Thompson (2009) to 0.002 mag rms, corresponding to 0.2 % (Fig. 4). The previous cycle of the 1970's and 1980's had a 40 % larger amplitude than the cycle where the HST data were obtained. The simplest adjustment of our seasonal model for the earlier cycle is increasing the $D2$ amplitude parameter by 40 %. In the earlier cycle, the brightness at green wavelengths (551 nm) stayed six years above its mean but more than eight years below (Lockwood and Thompson 2009) indicating deviations from our idealized sine curve model.

Our seasonal model includes high latitudes during the winter darkness that are difficult to observe, in particular the strongly negative values of $B1$ and $B2$ near -4. It seems unlikely that aerosol opacities get as small as suggested by the seasonal model. The observed ranges of $B1$ and $B2$ displayed in Figs. 9 and 10 stay above -1 and -2, respectively. The seasonal model is an

extrapolation of limited data that needs to be verified. In the darkness of winter, aerosols can still be probed in emission with Cassini's Composite Infrared Spectrometer (CIRS). Observations by Vinatier *et al.* (2015) indicated low haze extinction coefficients at high southern latitudes from 2009 to 2011, in qualitative agreement with our seasonal model, although it is unknown whether the aerosol opacities at wavelengths separated by a factor of 10 go hand in hand. Earlier CIRS data between 2004 and 2008 (Vinatier *et al.* 2010), probing near 160 km altitude, indicated a roughly constant haze extinction coefficient northward of 5° latitude but linearly decreasing to the south, qualitatively consistent with our high altitude model for the same period.

Cassini VIMS data taken at the end of 2006 analyzed by Rannou *et al.* (2010) show a latitudinal profile of the haze opacity that increases almost linearly from -80° to the equator, then is levelled to 30° and decreases slightly to 60° . This is very similar to the latitudinal shape of the second principal component at that date except that the model does not have the decrease above 30° . The observed variation is only half as large as ours, which corresponds to altitudes above 150 km. Rannou *et al.* (2010) estimate that their data corresponds to the optical depth above 100 km altitude. The altitude range of 100-150 km does not vary with time in our model and contains about as much haze optical depth as all altitudes above 150 km. Thus, even the apparent size discrepancy by a factor of two is explained. These VIMS profiles come from data between 1.7 and $3.5\ \mu\text{m}$ wavelength and are thus closer to our spectral range than the CIRS data near $9\ \mu\text{m}$.

Since the haze is influenced by the dynamics in Titan's atmosphere, one can compare our simple seasonal model of the haze with other parameters probing the circulation. Tokano *et al.* (1999) used a GCM to show that seasonal temperature variations at 1 mb pressure (~ 180 km altitude) are expected to have a flatter maximum and a sharper minimum. The measured distribution of trace gases with Cassini CIRS (Teanby *et al.* 2008, 2009) indicated latitudinal structure that is more complicated than the simple model presented here, but also showed very little temporal variation in the lower stratosphere where the presented model has no change in the

haze either, at least within the 80-150 km altitude range.

6. Summary

We analyzed spatially resolved Titan spectrophotometry collected by STIS in five years over a 7-year period to create five image cubes, each consisting of an image of Titan at ~1000 wavelengths between 530 and 1020 nm. We took special effort in the calibration process to extract variations as small as 0.001 in reflectivity. This is a strength of our data set compared to ground-based observations taken through a variable Earth's atmosphere, and compared to Cassini observation with constantly changing phase angles.

The ~1 million original data points were grouped and averaged into 2500 reduced data points, a four-dimensional data set of 25 spectral bands, 10 latitude regions, five dates, and two viewing angles. A principal component analysis characterized the significant features in this data set. We found two large, distinct components indicating major changes of Titan's haze. A small third component indicated a non-linearity effect of the first one. A fourth component described changing surface features due to Titan's rotation.

Radiative transfer models revealed the physical variations in Titan's atmosphere:

1. The first principal component is due to a change in haze opacity or a change in the shape of the phase function below 80 ± 20 km altitude. Residuals are very low if both physical parameters contribute. The variation appears to be stronger toward longer wavelengths suggesting a change of aerosol size too. A possible physical explanation is that gases, perhaps HCN, condense at around 80 km altitude onto aerosols and increase in size, and that the speed of condensation varies with location and seasons based on atmospheric dynamics.

2. The second principal component is due to a change of haze opacity at altitudes above 150 ± 50 km. It is probably driven by atmospheric dynamics moving aerosols. Variable speeds of

coagulation of aerosols may contribute, which is also influenced by dynamics. Both principal components together characterize Titan's seasonal north-south asymmetry that is well known, including its wavelength dependent phasing (Lorenz *et al.* 1997, 1999, 2001, 2004, 2006), but its separation into two distinct components is new.

3. We did not detect any temporal or latitudinal change of the haze between 80 and 150 km altitude.

4. The tropics have significantly larger haze opacity at high altitudes (>150 km) but slightly reduced opacity at low altitudes (<80 km) compared to the global average.

5. The high-altitude haze opacity was symmetric with respect to the Equator at the end of 2001, at which point its north-south asymmetry reversed. The data are consistent with all latitudes switching asymmetry at the same time, but the constraint is weak. The opposite season will occur in spring 2016, when the next reversal may take place.

6. The asymmetry reversal for the low-altitude haze opacity occurred later than at high altitudes, for tropical latitudes in the middle of 2002, for mid latitudes in 2003, and high latitudes about early 2004. The next reversal may occur throughout 2017 and 2018. The last reversal in this direction occurred sometimes between 1981 (Voyager 2) and 1990 (HST).

7. Amplitudes of temporal variations for both principal components increase almost linearly with distance from the Equator.

8. The data can be fit well by assuming that all observed variations are purely seasonal with shapes of sine curves. This seasonal model completely describes Titan's haze parameters at each altitude, latitude, and time (Table 6). While the model fits the data between 1997 and 2004, it also is roughly consistent with a number of Cassini observations made since 2004 (cf. Sections 4.3 and 5.3). The model may be an approximate description of Titan's seasonal haze cycle that changed significantly from the last cycle to the current one (Lockwood and Thompson 2009).

[Table 6 approximately here]

Our model provides more realistic atmospheric corrections in photometric investigations of Titan's surface than using a constant model such as the DISR haze model that was determined at a specific date and latitude. The three parameters of our seasonal model, mean values, amplitudes, and phasing, and their variations with latitude can be compared with studies of Global Circulation Models leading to a better understanding of Titan's seasonal cycle.

Acknowledgements

This work was supported by the STScI through Archive Research program AR 12624. The contribution of Caitlin Griffith, the principal investigator for this program, is appreciated. This work was based on HST data from observations with Principal Investigators Mark Lemmon, Caitlin Griffith, and Eliot Young. Support for HST was provided by NASA through the Space Telescope Science Institute, which is operated by the Association of Universities for Research in Astronomy, Incorporated, under NASA contract NAS5-26555.

References

- Ádámkovics, M., de Pater, I., Hartung, M., Eisenhauer, F., Genzel, R. 2006. Titan's bright spots: multiband spectroscopic measurement of surface diversity and hazes. *J. Geophys. Res.* **111**, E07S06.
- Brown, R.H., and 25 colleagues 2006. Observations in the Saturn system during approach and orbital insertion, with Cassini's visual and infrared mapping spectrometer (VIMS). *Astron. Astrophys.* **446**, 707-716.
- Caldwell, J.D., Smith, P.H., Tomasko, M.G., McKay, C.P. 1992. Titan: evidence of seasonal change—A comparison of Voyager and Hubble Space Telescope images. *Icarus* **103**, 1-9.
- Colina, L., Bohlin, R.C., Castelli, F. 1996. The 0.12-2.5 micron absolute flux distribution of the Sun for comparison with solar analog stars. *Astronom. J.* **112**, 307-315.
- Coustenis, A., Gendron, E., Lai, O., Véran, J.-P., Woillez, J., Combes, M., Vapillon, L., Fusco, T., Mugnier, L., Rannou, P. 2001. Images of Titan at 1.3 and 1.6 μm with adaptive optics at the CFHT. *Icarus* **154**, 501-515.
- Crespin, A., Lebonnois, S., Vinatier, S., Bézard, B., Coustenis, A., Teanby, N.A., Achterberg, R.K., Rannou, P., Hourdin, F. 2008. Diagnostics of Titan's stratospheric dynamics using Cassini/CIRS data and the two-dimensional IPSL circulation model. *Icarus* **197**, 556-571.
- de Kok, R., Irwin, P.G.J., Teanby, N.A., Vinatier, S., Tosi, F., Negrão, A., Osprey, S., Ardiani, A., Moriconi, M.L., Coradini, A. 2010. A tropical haze band in Titan's stratosphere. *Icarus* **207**, 485-490.
- Doose, L.R., Karkoschka, E., Tomasko, M. 2015. Vertical structure and optical properties

of Titan's aerosols from measurements made inside and outside the atmosphere. Submitted to *Icarus*.

Ely, J., Aloisi, A., Bohlin, R., Bostroem, A., Diaz, R., Dixon, V., Goudfrooij, P. Hodge, P., Lennon, D., Long, C., Niemi, S., Osten, R., Proffitt, C., Walborn, N., Wheeler, T., Wolfe, M., York, B., Zheng, W., 2011. *STIS Instrument Handbook*, Version 11.0, STScI, Baltimore.

Goudfrooij, P., Kimble, R.A. 2002. Correcting STIS CCD photometry for CTE loss. 2002 *HST calibration Workshop*, Arribas, S., Koekemoer, A., Whitmore, B. eds., STScI, Baltimore.

Goudfrooij, P., Maíz-Apellániz, J., Brown, T., Kimble, R. 2006. Charge transfer efficiency of the STIS CCD: The time dependence of charge loss and centroid shifts from Internal Sparse Field data. Instrument Science Report STIS 2006-01, STScI, Baltimore.

Hirtzig, M., Coustenis, A., Gendron, E., Drossart, P., Negrão, A., Combes, M., Lai, O., Rannou, P., Lebennois, S., Luz, D. 2006. Monitoring atmospheric phenomena on Titan. *Astron. Astrophys.* **456**, 761-774.

Karkoschka, E. 1994. Spectrophotometry of the Jovian planets and Titan at 300- to 1000-nm wavelength: the methane spectrum. *Icarus* **111**, 174-192.

Karkoschka, E. 1998. Methane, ammonia, and temperature measurements of the jovian planets and Titan from CCD-spectrophotometry. *Icarus* **133**, 134-146.

Karkoschka, E., Lorenz, R.D. 1996. Latitudinal variation of aerosol sizes inferred from Titan's shadow. *Icarus* **125**, 369-379.

Karkoschka, E., Tomasko, M. 2009. The haze and methane distributions on Uranus from HST-STIS spectroscopy. *Icarus* **202**, 287-309.

Karkoschka, E., Tomasko, M.G. 2010. Methane absorption coefficients for the jovian planets from laboratory, Huygens, and HST data. *Icarus* **205**, 674-694.

- Krist, J. 2004. *The Tiny Tim User's Guide, Version 6.3*. Space Telescope Science Institute, Baltimore.
- Lavvas, P., Griffith, C.A., Yelle, R.V. 2011. Condensation in Titan's atmosphere at the Huygens landing site. *Icarus* **215**, 732-750.
- Lockwood, G.W. 1977. Secular brightness increases of Titan, Uranus, and Neptune, 1972-1976. *Icarus* **32**, 413-430.
- Lockwood, G.W., Thompson, D.T. 2009. Seasonal photometric variability of Titan, 1972-2006. *Icarus* **200**, 616-626.
- Lora, J.M., Lunine, J.I., Russell, J.L. 2015. GCM simulations of Titan's middle and lower atmosphere and comparison to observations. *Icarus* **250**, 516-528.
- Lorenz, R.D., Smith, P.H., Lemmon, M.T., Karkoschka, E., Lockwood, G.W., Caldwell, J. 1997. Titan's north-south asymmetry from HST and Voyager imaging: comparison with models and ground-based photometry. *Icarus* **127**, 173-189.
- Lorenz, R.D., Lemmon, M.T., Smith, P.H., Lockwood, G.W. 1999. Seasonal change observed on Titan's with the Hubble Space Telescope WFPC-2. *Icarus* **142**, 391-401.
- Lorenz, R.D., Young, E.F., Lemmon, M.T. 2001. Titan's smile and collar: HST observations of seasonal change 1994-2000. *Geophys. Res. Lett.* **28**, 4453-4456.
- Lorenz, R.D., Smith, P.H., Lemmon, M.T. 2004. Seasonal change in Titan's haze 1992-2002 from Hubble Space Telescope observations. *Geophys. Res. Lett.* **31**, L10702.
- Lorenz, R.D., Lemmon, M.T., Smith, P.H. 2006. Seasonal evolution of Titan's dark polar hood: midsummer disappearance observed by the Hubble Space telescope. *Monthly Notices Royal Astron. Soc.* **369**, 1683-1687.
- McGrath, M.A., Hodge, P., Baum, S. 1998. Calstis7: Two-dimensional rectification of

spectroscopic data in the STIS calibration pipeline. Instrument Science Report STIS 98-13. STScI, Baltimore.

Penteado, P.F., Griffith, C.A., Tomasko, M.G., Engel, S., See, C., Doose, L., Baines, K.H., Brown, R.H., Buratti, B.J., Clark, R., Nicholson, P., Sotin, C. 2010. Latitudinal variations in Titan's methane and haze from Cassini VIMS observations. *Icarus* **206**, 352-365.

Porco, C.C., and 35 colleagues 2005. Imaging of Titan from the Cassini spacecraft. *Nature* **434**, 159-168.

Quijano, K., Aloisi, A., Brown, T., Busko, I., Davies, J., Diaz-Millaer, A., Dressel, L., Goudfrooij, P., Hodge, P., Hofeltz, S., Kaiser, M.E., Apellániz, J.M., Mobasher, B., Proffitt, C., Sahu, K., Stys, D., Walborn, N. 2007. STIS Instrument Handbook, Version 8.0. Space Telescope Science Institute, Baltimore, Maryland.

Rannou, P., Hourdin, F., McKay, C.P., Luz, D. 2004. A coupled dynamics-microphysics model of Titan's atmosphere. *Icarus* **170**, 443-462.

Rannou, P., Cours, T., Le Mouélic, S., Rodriguez, S., Sotin, C., Drossart, P., Brown, R. 2010. Titan haze distribution and optical properties retrieved from recent observations. *Icarus* **208**, 850-867.

Roe, H.G., de Pater, I., Macintosh, B.A., Gibbard, S.G., Max, C.E., McKay, C.P. 2002. Titan's atmosphere in late southern spring observed with adaptive optics on the W. M. Keck II 10-meter telescope. *Icarus* **157**, 254-258.

Smith, B.A., Soderblom, L.A., Beebe, R., Boyce, J., Briggs, G., Bunker, A., Collins, S.A., Hansen, C.J., Johnson, T.V., Mitchell, J.L., Terrile, R.J., Carr, M., Cook II, A.F., Cuzzi, J., Pollack, J.B., Danielson, G.E., Ingersoll, A., Davies, M.E., Hunt, G.E., Masursky, H., Shoemaker, E., Morrison, D., Owen, T., Sagan, C., Veverka, J., Strom, R., Suomi, V. 1981.

Encounter with Saturn: Voyager 1 imaging results. *Science* **212**, 163-182.

Smith, B.A., Soderblom, L.A., Batson, B., Bridges, P., Inoe, J., Masursky, H., Shoemaker, E., Beebe, R., Boyce, J., Briggs, G., Bunker, A., Collins, S.A., Hansen, C.J., Johnson, T.V., Mitchell, J.L., Terrile, R.J., Carr, M., Cook II, A.F., Cuzzi, J., Pollack, J.B., Danielson, G.E., Ingersoll, A., Davies, M.E., Hunt, G.E., Morrison, D., Owen, T., Sagan, C., Veverka, J., Strom, R., Suomi, V. 1982. A new look at the Saturn system: The Voyager 2 images. *Science* **215**, 504-537.

Sromovsky, L.A., Suomi, V.E., Pollack, J.B., Kraus, R.J., Limaye, S.S., Owen, T., Revercomb, H.E., Sagan, C. 1981. Implications of Titan's north-south brightness asymmetry. *Nature* **292**, 698-702.

Sromovsky, L.A., Lockwood, G.W., Thompson, D.T. 1986. Titan's albedo variation: Relative influence of solar UV and seasonal contrast mechanism. *Bull. Am. Astron. Soc.* **18**, 809.

Teanby, N.A., Irwin, P.G.J., de Kok, R., Nixon, C.A., Coustenis, A., Royer, E., Calcutt, S.B., Bowles, N.E., Fletcher, L., Howett, C., Taylor, F.W. 2008. Global and temporal variations in hydrocarbons and nitriles in Titan's stratosphere for northern winter observed by Cassini/CIRS. *Icarus* **193**, 595-611.

Teanby, N.A., Irwin, P.G.J., de Kok, R., Nixon, C.A. 2009. Dynamical implications of seasonal and spatial variations in Titan's stratospheric composition. *Phil. Trans. Roy. Soc.* **367**, 697-711.

Teanby, N.A., Irwin, P.G.J., Nixon, C.A., de Kok, R., Vinatier, S., Coustenis, A., Sefton-Nash, E., Calcutt, S.B., Flasar, F.M. 2012. Active upper-atmosphere chemistry and dynamics from polar circulation reversal on Titan. *Nature* **491**, 732-735.

Tokano, T., Neubauer, F.M., Laube, M., McKay, C.P. 1999. Seasonal variation of Titans atmospheric structures simulated by a general circulation model. *Planet. Space Sci.* **47**, 493-520.

Tomasko, M.G., and 39 colleagues 2005. Rain, winds and haze during the Huygens probe's descent to Titan's surface. *Nature* **438**, 765-778.

Tomasko, M.G., Doose, L., Engel, S., Dafoe, L.E., West, R., Lemmon, M., Karkoschka, E., See, C. 2008. A model of Titan's aerosols based on measurements made inside the atmosphere. *Planet. Space Sci.* **56**, 669-707.

Vinatier, S., Bézard, B., de Kok, R., Anderson, C.M., Samuelson, R.E., Nixon, C.A., Mamoutkine, A., Carlson, R.C., Jennings, D.E., Guandique, E.A., Bjoraker, G.L., Flasar, F.M., Kunde, V.G. 2010. Analysis of Cassini/CIRS limb spectra acquired of Titan during the nominal mission II: aerosol extinction profiles in the 600-1420 cm^{-1} spectral range. *Icarus* **210**, 852-866.

Vinatier, S., Bézard, B., Lebonnois, S., Teanby, N.A., Achterberg, A.K., Gorius, N., Mamoutkine, A., Guandique, E., Jolly, A., Jennings, D.E., Flasar, F.M. 2015. Seasonal variation in Titan's middle atmosphere during the northern spring derived from Cassini/CIRS observations. *Icarus* **250**, 95-115.

Table 1: Observational parameters

Date, UT	L_s	lg(earth)	φ (earth)	φ (sun)	diameter	phase angle	# of exposures
	($^\circ$)	($^\circ$)	($^\circ$)	($^\circ$)	(arc-sec)	($^\circ$)	
1997-11-03.44	204	306	-9.4	-10.8	0.837	2.7	3
1999-10-07.95	229	319	-20.7	-19.9	0.851	3.3	18
2000-11-23.76	244	267	-23.6	-23.8	0.873	0.6	19
2002-11-27.55	272	241	-26.4	-26.6	0.875	2.4	9
2004-01-03.42	287	300	-25.5	-25.4	0.881	0.3	7

Note: lg and φ are sub-earth/sub-solar longitudes and latitudes, respectively. L_s is the solar longitude relative to the spring equinox.

Table 2: Principal component amplitudes A1 and A2

Wavelength	$\kappa(\text{CH}_4)$	amplitude A1		amplitude A2	
nm	km-am ⁻¹	$\mu=0.6$	$\mu=0.8$	$\mu=0.6$	$\mu=0.8$
543	0.03	-0.0008	-0.0001	-0.0036	-0.0070
543	0.10	-0.0007	0.0004	-0.0031	-0.0063
576	0.03	0.0003	0.0016	-0.0040	-0.0073
619	0.03	0.0019	0.0043	-0.0036	-0.0063
619	0.10	0.0024	0.0051	-0.0031	-0.0059
619	0.32	0.0029	0.0064	-0.0016	-0.0037
666	0.03	0.0038	0.0079	-0.0023	-0.0046
666	0.10	0.0044	0.0089	-0.0016	-0.0037
727	0.03	0.0064	0.0120	-0.0009	-0.0028
727	0.10	0.0072	0.0129	-0.0002	-0.0020
727	0.32	0.0077	0.0134	0.0008	-0.0010
727	1.0	0.0070	0.0122	0.0028	0.0016
727	3.2	0.0043	0.0079	0.0056	0.0050
793	0.03	0.0086	0.0146	0.0006	-0.0014
793	0.10	0.0097	0.0154	0.0009	-0.0010
793	0.32	0.0104	0.0159	0.0020	0.0002
793	1.0	0.0095	0.0146	0.0038	0.0024
890	0.03	0.0108	0.0164	0.0012	-0.0003
890	0.10	0.0119	0.0175	0.0020	0.0004
890	0.32	0.0125	0.0171	0.0024	0.0008
890	1.0	0.0111	0.0146	0.0036	0.0018
890	3.2	0.0066	0.0090	0.0057	0.0040
890	10	0.0023	0.0040	0.0069	0.0058
890	32	-0.0002	0.0006	0.0068	0.0058
990	10	0.0040	0.0044	0.0059	0.0044

Note: Bands are identified by the listed central wavelength and the methane absorption coefficient $\kappa(\text{CH}_4)$.

Table 3: Principal component values B1

Latitude	1997	1999	2000	2002	2004
-65°	3.04	2.99	2.11	0.65	0.01
-55°	2.83	2.70	1.87	0.63	-0.08
-45°	2.16	1.96	1.23	0.32	-0.15
-35°	1.12	1.03	0.53	-0.22	-0.30
-25°	0.32	0.29	-0.04	-0.57	-0.65
-15°	0.04	-0.28	-0.48	-0.71	-0.94
-5°	-0.45	-0.58	-0.79	-0.68	-1.11
5°	-0.88	-0.74	-1.04	-0.63	-1.04
15°	-1.36	-0.82	-1.10	-0.43	-0.75
25°	-1.54	-0.70	-1.05	-0.26	-0.49

Table 4: Principal component values B2

Latitude	1997	1999	2000	2002	2004
-65°	0.17	0.37	-0.81	-2.09	-2.45
-55°	0.32	0.31	-0.85	-2.01	-2.45
-45°	0.35	0.38	-0.62	-1.79	-1.87
-35°	0.51	0.46	-0.32	-1.35	-1.37
-25°	0.76	0.74	0.31	-0.74	-0.72
-15°	0.93	1.04	0.87	-0.01	0.17
-5°	0.92	1.05	1.01	0.74	0.94
5°	0.54	0.64	0.86	1.00	1.36
15°	-0.41	-0.21	0.32	0.90	1.49
25°	-1.54	-1.34	-0.40	0.61	1.37

Table 5: Haze opacity factors

$B1, B2$	factor for $B1$	factor for $B2$
----------	--------------------	--------------------

-4.0	0.09	0.12
-3.5	0.23	0.22
-3.0	0.37	0.33
-2.5	0.53	0.43
-2.0	0.68	0.54
-1.5	0.84	0.65
-1.0	1.00	0.77
-0.5	1.17	0.88
0.0	1.34	1.00
0.5	1.51	1.12
1.0	1.69	1.25
1.5	1.88	1.38
2.0	2.08	1.51
2.5	2.28	1.65
3.0	2.49	-
3.5	2.71	-
4.0	2.94	-

Table 6: Our seasonal haze model

Haze parameters from Doose *et al.* (2015), except:

- 1) altitudes 0-80 km: multiply haze opacities within this layer by the opacity factor for $B1$ (cf. Table 5) where $B1$ is calculated by Eq. 3 from $M1$, $D1$, and $E1$, and these parameters as function of latitude are taken from Fig. 14 (for a southern latitude, use the symmetric northern one and change the sign of $D1$),
- 2) altitudes 80-150 km remain unchanged,
- 3) altitudes above 150 km: multiply haze opacity within this layer by the opacity factor for $B2$ (cf. Table 5) where $B2$ is calculated by Eq. 3 from $M2$, $D2$, and $E2$, similar to low altitudes.

Fig. 1: The original data of the 10 exposures of 2002, from top to bottom. Nine exposure were on Titan, from limb to limb, and the last exposure was a lamp flatfield. The top and bottom spectra probe the SW and NE limbs, respectively. The spatial direction (down-up) corresponds to NW-SE on Titan. The spectral direction goes from left to right. Two solar lines and three main methane bands are indicated.

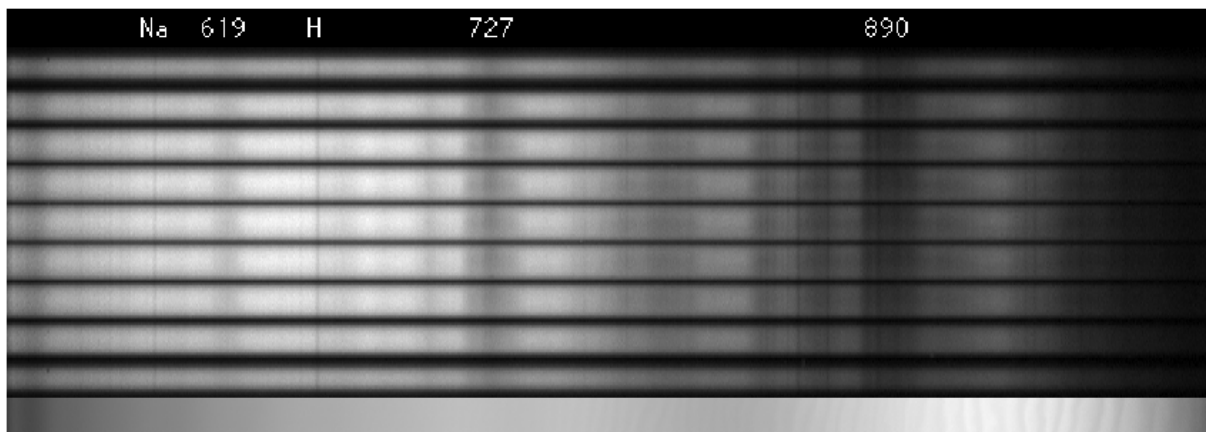


Fig. 2: The geometry for all slit positions on Titan's disk, shown for each observing date. North on Titan is oriented upwards in each image. The center of the disk (sub-Earth point) is marked by a cross, the sub-solar point by a circle. The nine shown latitude circles go from 60° South to 20° North every 10° . They are the boundaries between the 10 latitude regions of this work.

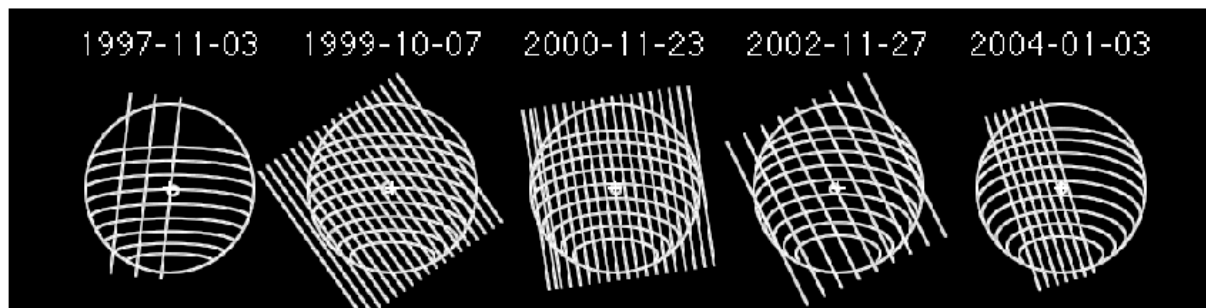



Fig. 3: Spectral calibration (top) and spatial navigation (bottom). The measurements are shown by solid dots, averages between top and bottom data points as open circles. The first exposure of 1999 is not shown since it was positioned off the disk of Titan. Curves are adopted fits. 

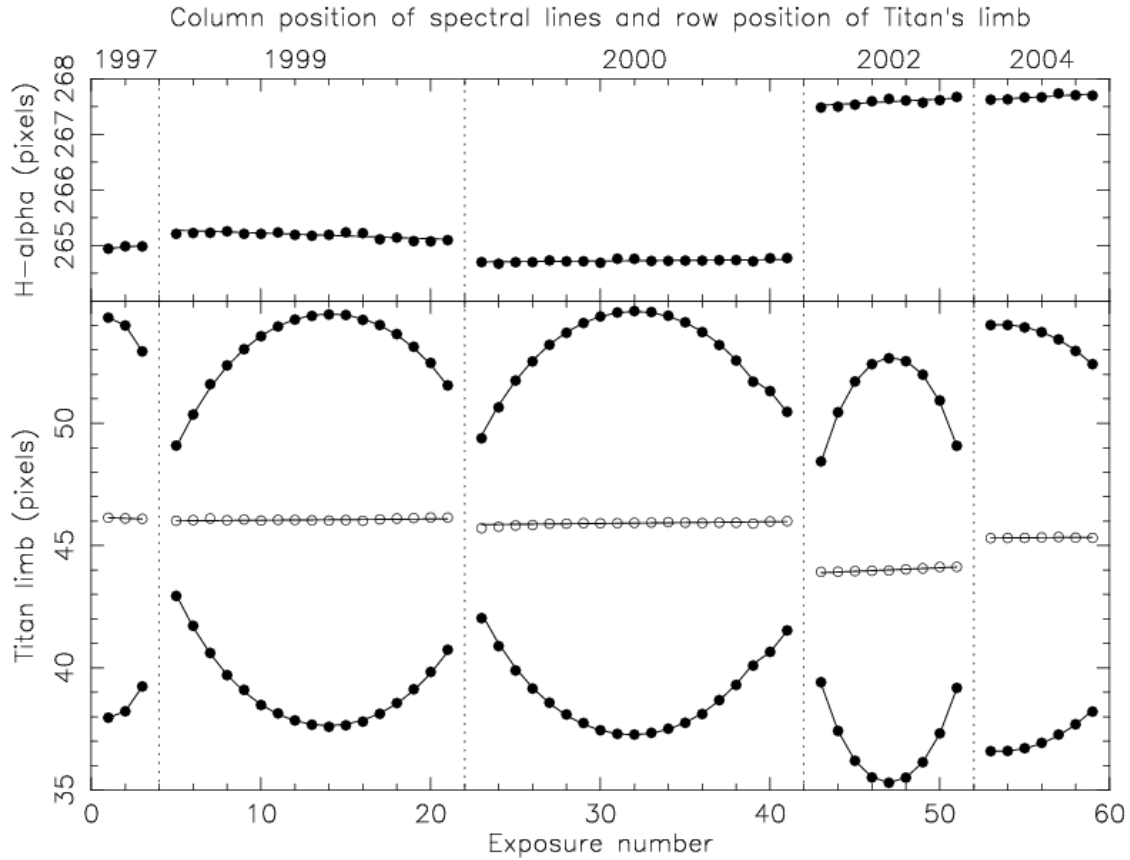


Fig. 4: Comparison of absolute intensity calibration in the y passband. The solid line and symbols come from different investigations as shown. Error bars from Lockwood and Thompson (2009) are shown as dotted lines. The symbols indicate a smoother variation than the solid line, but both are consistent with each other. The spacing of vertical tick marks corresponds to 0.9 % in intensity.

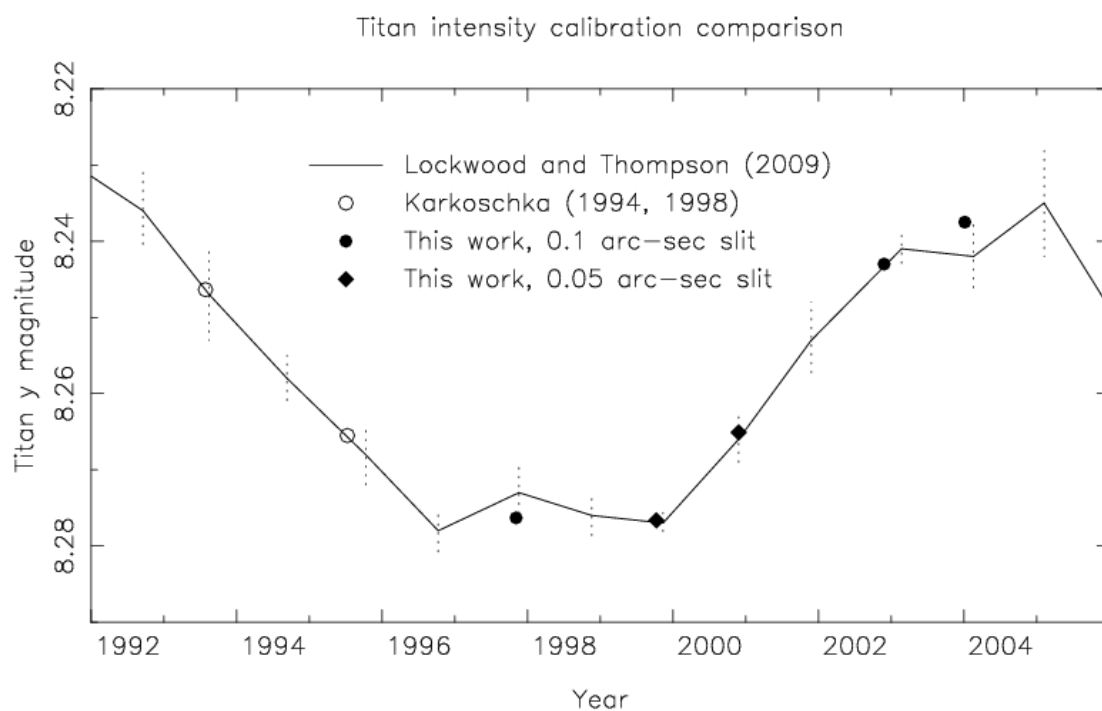


Fig. 5: The geometric albedo spectrum of Titan (bottom) and its limb darkening ratio (top), the reflectivity ratio between $\mu = 0.8$ and $\mu = 0.6$. The solid spectrum is the average from this work, the dotted spectrum from Karkoschka (1998). Vertical dotted lines separate the eight wavelength regions with the central methane band wavelength (nm) listed on top. Symbols mark averages within each wavelength region for the listed methane absorption coefficients in $(\text{km}\cdot\text{am})^{-1}$ as shown by the symbols. The dashed curve at the bottom shows the influence of Titan's surface albedo on its geometric albedo if Titan's surface had the reflectivity of its brightest versus its darkest spot.

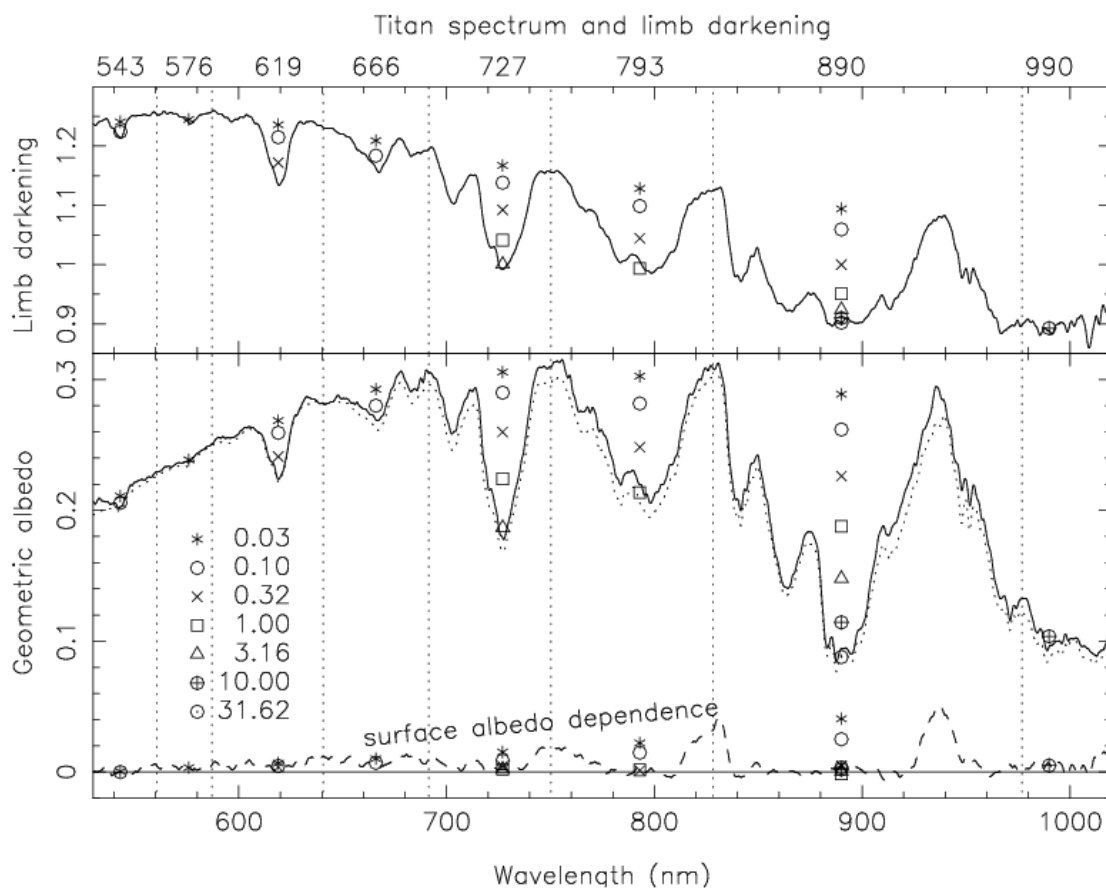


Fig. 6: Titan images for our 25 spectral bands, combinations of central wavelength and methane absorption coefficient listed on top, and five observing sessions listed on the left side. To better display small variations, an average intensity distribution shown in the top row was subtracted before the difference was displayed with quadruple contrast. The coverage of Titan's disk in 1997 and 2004 is partial (cf. Fig.2). The column at right shows Titan surface albedo features measured by Cassini ISS. These images were created from a longitude-latitude map at higher spatial resolution released 2011-10-26 by NASA/JPL-Caltech/Space Science Institute. The bottom four rows show contributions from the first two principal components to Titan's disk reflectivity in 1999 and 2002.

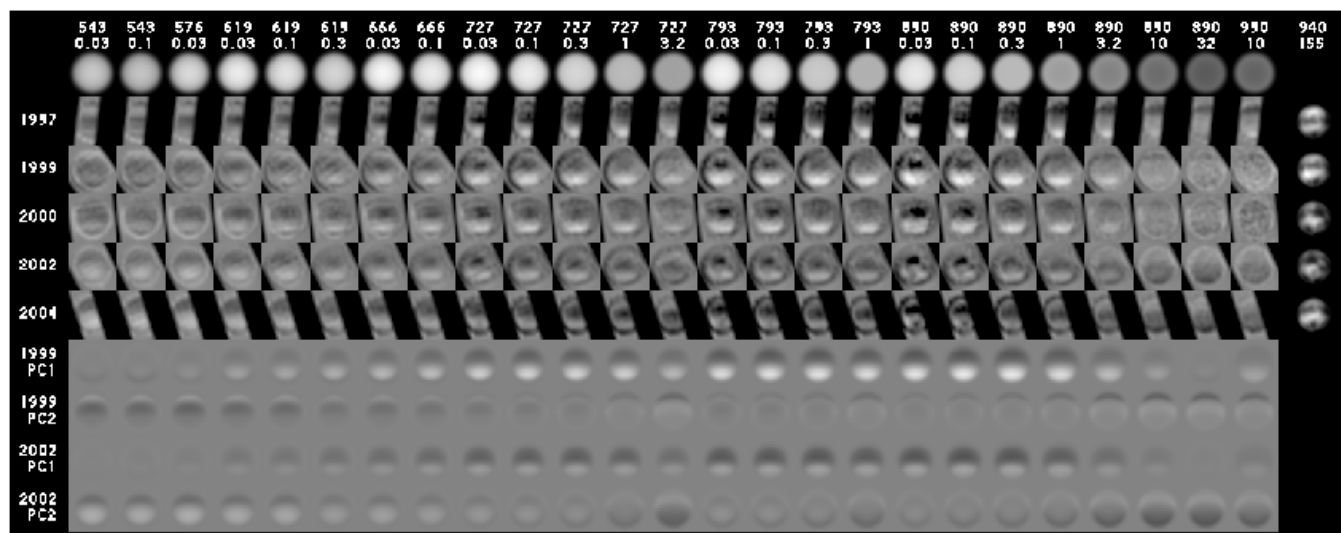


Fig. 7: Amplitudes of the principal component amplitudes $A1$ (top), $A2$ (center), and $A3$ (bottom), ordered first according to methane absorption coefficient (top of each panel in $(\text{km}\cdot\text{am})^{-1}$), and then according to wavelength (bottom scale). Solid dots and curves refer to $\mu = 0.8$, while open circles and dotted curves refer to $\mu = 0.6$.

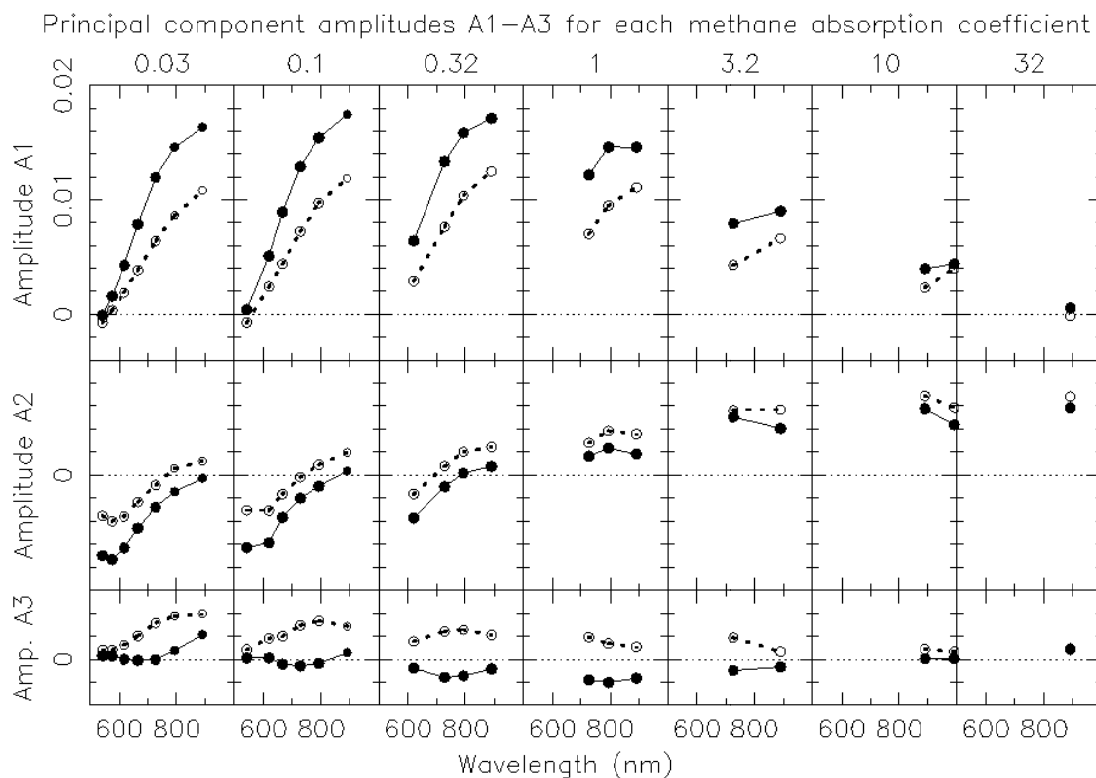


Fig. 8: Models of increased haze opacity (curves) below 80 km altitude by 34 % (top panel) and above 150 km by 25 % (bottom panel) compared to observed amplitudes for the first two principal components (symbols). Solid dots and curves are for $\mu = 0.8$, open circles and dotted curves for $\mu = 0.6$. Spectral bands are identified by the central wavelength (top) and methane absorption coefficient (bottom scale).

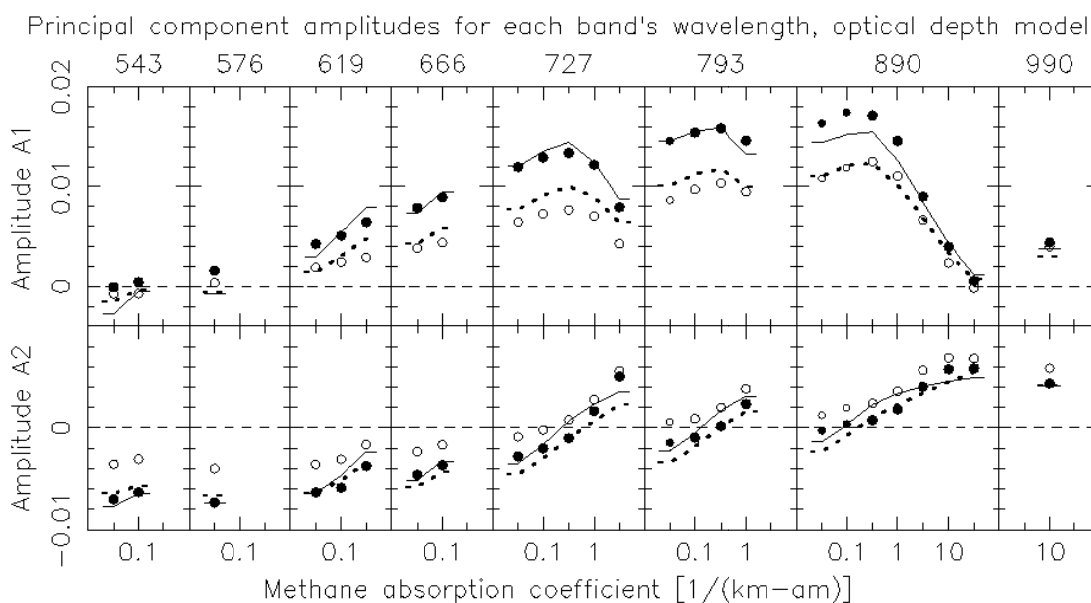


Fig. 9: Principal component values $B1$ (top), $B2$ (middle) and $B3$ (bottom), ordered first according to latitude (top of each panel), and then according to observing date (bottom scale with tick marks every year). Dots sizes indicate the number of original observations with a factor of about 25 between the largest and smallest dots, corresponding to five-fold larger uncertainties for the smallest dots compared to the largest ones.

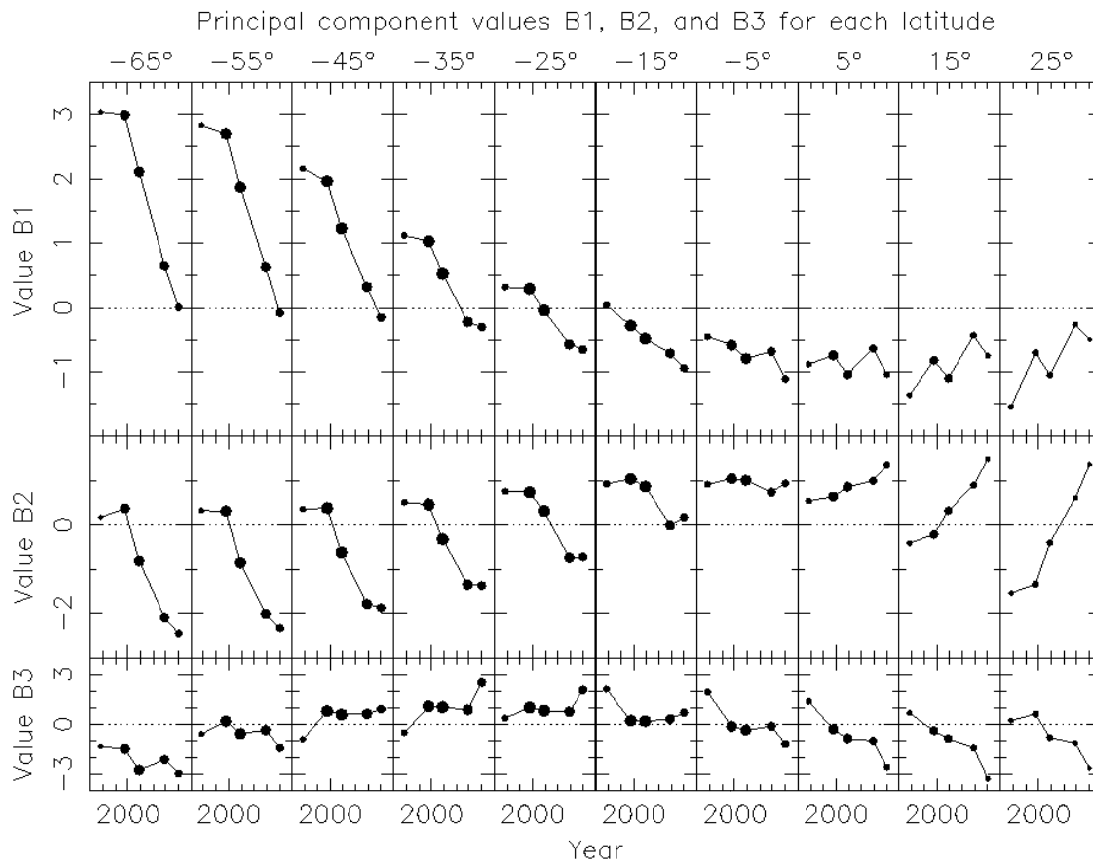


Fig. 10: Principal component values $B1$ (top) and $B2$ (bottom), ordered first according to observing date (top of each panel), and then according to latitude (bottom scale). Curves are for the seasonal model.

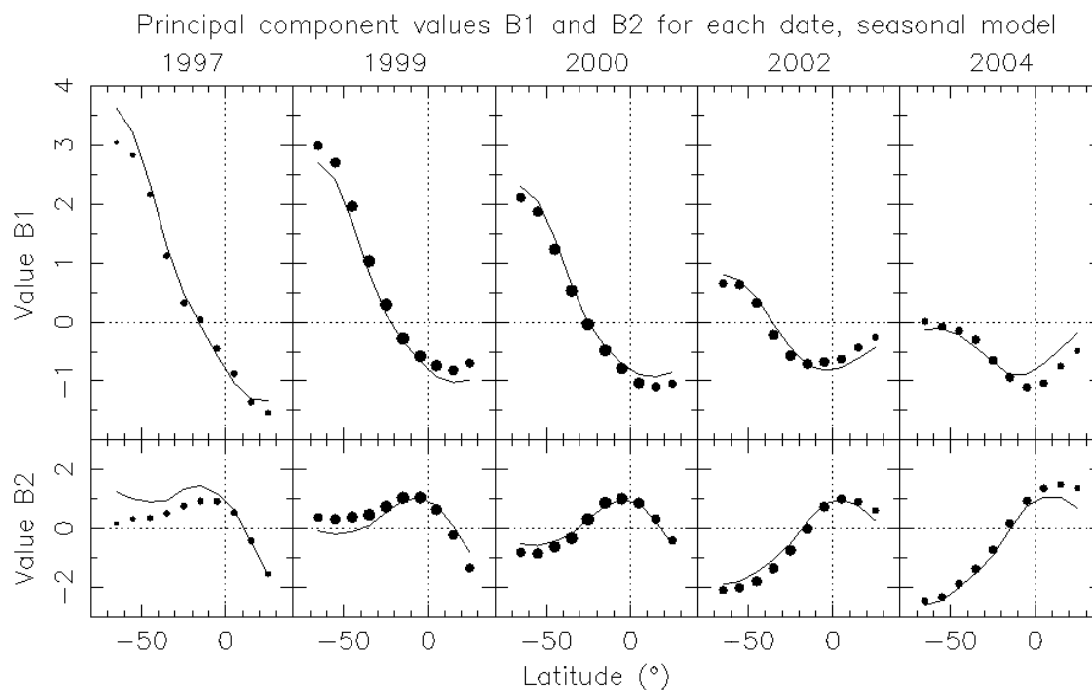


Fig. 11: Models (curves) and observations (dots) as function of methane absorption coefficient for the first (A1, top panels) and second principal component amplitudes (A2, bottom panels) within the 890 nm spectral band. The altitude regions of increased haze opacity are listed in each panel. Solid curves and dots are for the geometry $\mu = 0.8$, dashed curves and open circles are for the geometry $\mu = 0.6$.

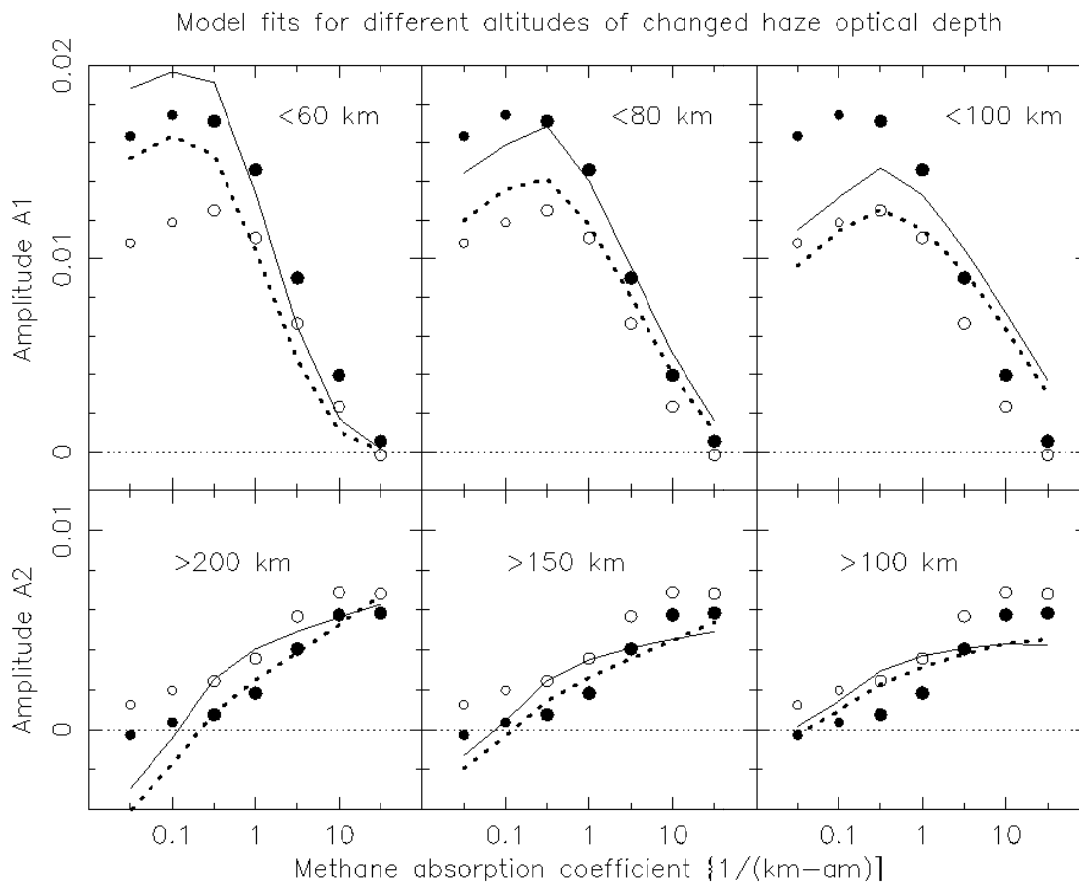


Fig. 12: Models of backward scattering phase functions below 80 km altitude (top panel) and above 150 km (bottom panel) compared to observed amplitudes of the first two principal components. Symbols are the same as in Figs. 7, 8, and 11. Spectral bands are identified by the central wavelength (top) and methane absorption coefficient (bottom scale).

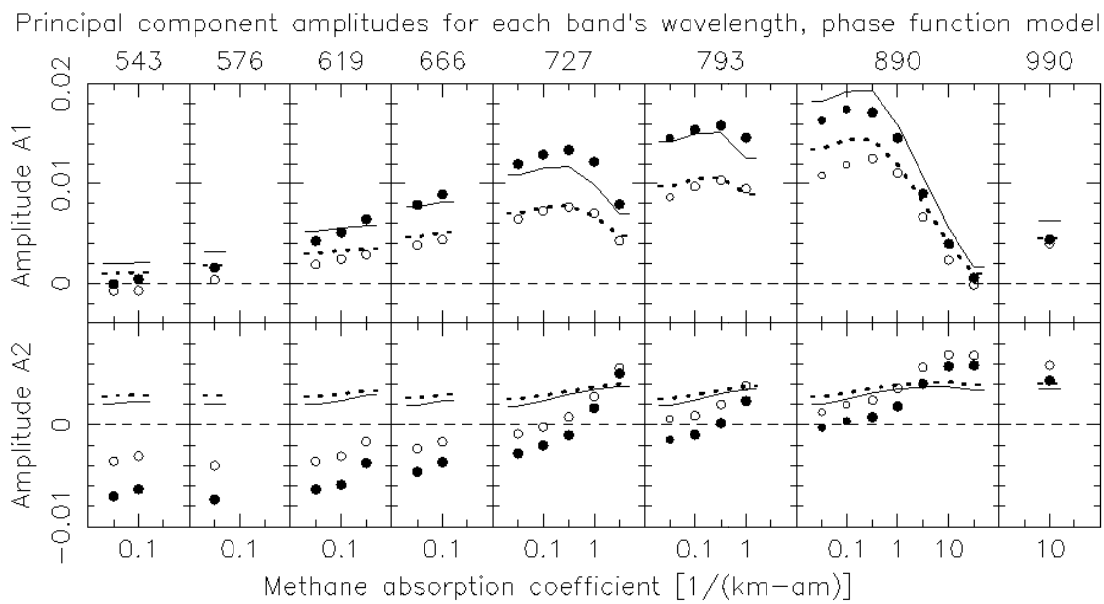


Fig. 13: Models of increased single scattering albedos below 80 km altitude (top panel) and above 150 km (bottom panel) compared to observed amplitudes of the first two principal components. Symbols are the same as in Figs. 7, 8, and 11. Spectral bands are identified by the central wavelength (top) and methane absorption coefficient (bottom scale).

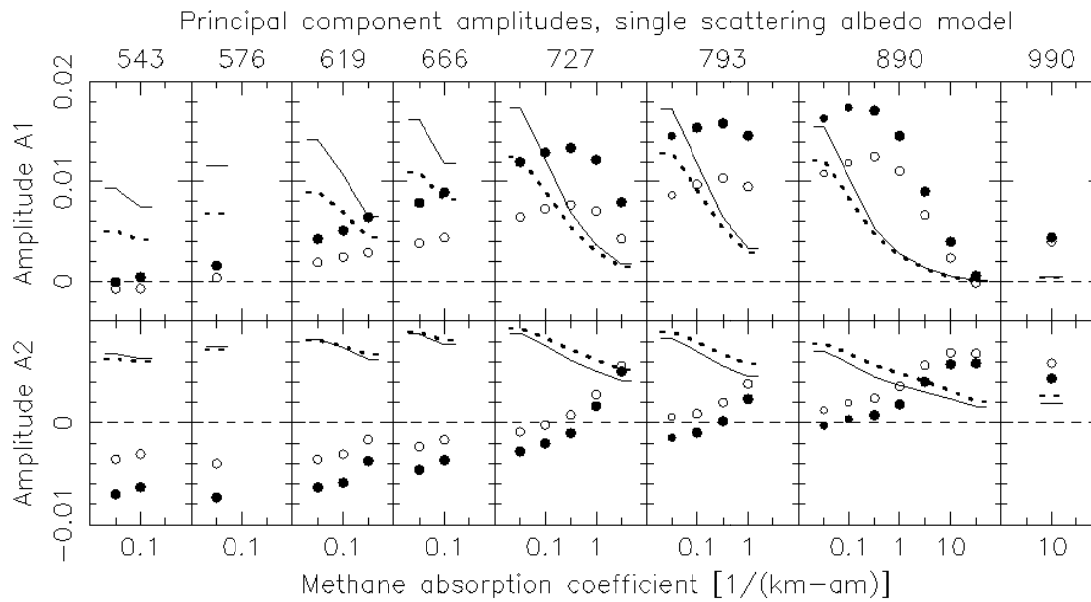


Fig. 14: The three parameters of the seasonal model for the first (solid dot and curves) and second principal component (open squares and dashed curves), each as function of latitude according to Eq. 3. Southern latitudes are assumed symmetric to northern ones, except for a change of sign for $D1$ and $D2$.

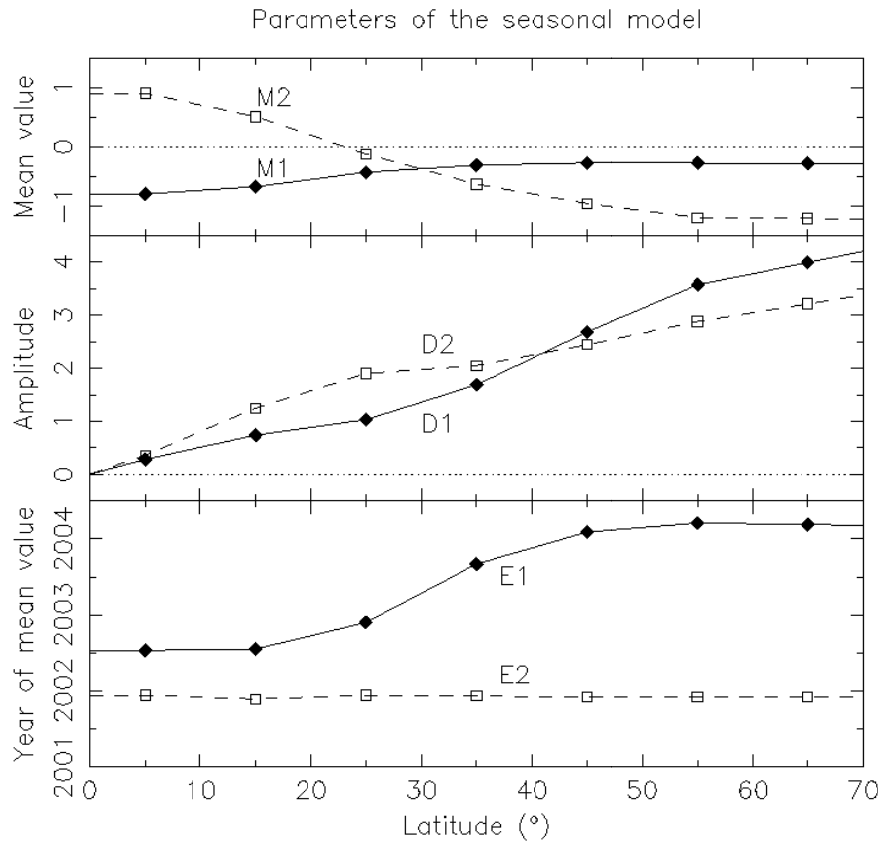
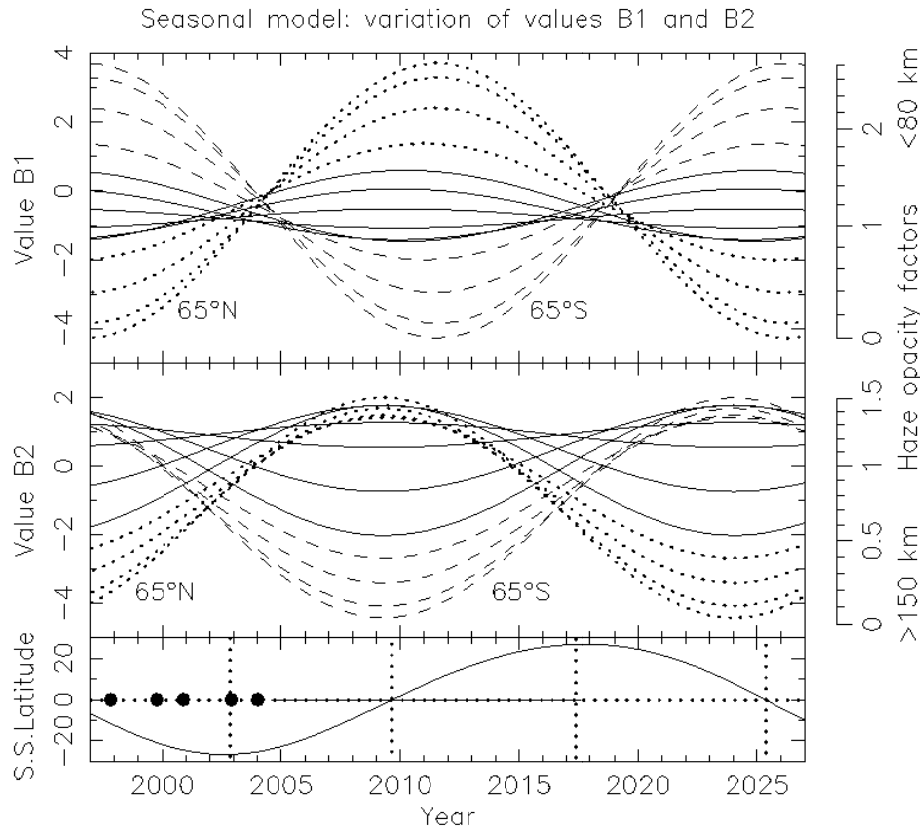


Fig. 15: The variation of values $B1$ (top) and $B2$ (middle) as function of time over a whole Titan year for 14 latitudes from -65° to 65° latitude, every 10° . The six latitudes within 30° of the Equator are shown as solid curves, the ones further north and south as dotted and dashed, respectively. The bottom panel shows the sub-solar latitude. The five dots indicate the dates for our observations, the horizontal bar the planned duration of the Cassini mission at Saturn, and the vertical dotted lines the equinoxes and solstices. The scales at the right show approximate haze opacity factors for altitudes below 80 km (top panel) and above 150 km (middle panel).



- > HST-STIS image cubes in five years provide a unique probe of atmospheric variations.
- > The first principal component describes haze opacity variations below 80 km altitude.
- > The second one has similar variations above 150 km but its phase is 1-2 years ahead.
- > The tropics have higher (>150 km) and lower (<80 km) opacities than the global mean.
- > The north-south asymmetry may reverse in 2016 (>150 km) and 2017-2018 (<80 km).